Acta Cryst A FOUNDATIONS ADVANCES

ISSN 2053-2733

An algebraic approach to cooperative rotations in networks of interconnected rigid units

Branton Campbell,[a]* Christopher J. Howard,[b] Tyler B. Averett,[a] Thomas A. Whittle,[c]‡ Siegbert Schmid,[c] Shae Machlus,[a] Christopher Yost[a] and Harold T. Stokes[a]

[a]Department of Physics and Astronomy, Brigham Young University, Provo, Utah 84602, USA, [b]School of Engineering, The University of Newcastle, University Drive, Callaghan, NSW 2308, Australia, and [c]School of Chemistry, The University of Sydney, Sydney, NSW 2308, Australia. *Correspondence e-mail: branton_campbell@byu.edu

Received 7 November 2017
Accepted 7 July 2018

Edited by H. Schenk, University of Amsterdam, The Netherlands

‡ Current address: Materials Innovation Factory, University of Liverpool, Oxford Street, Liverpool L7 3NY, England.

Keywords: rigid-unit modes; cooperative rotations; group theory; symmetry modes; perovskites; quartz; tungsten bronzes.

Supporting information: this article has supporting information at journals.iucr.org/a

Crystalline solids consisting of three-dimensional networks of interconnected rigid units are ubiquitous amongst functional materials. In many cases, application-critical properties are sensitive to rigid-unit rotations at low temperature, high pressure or specific stoichiometry. The shared atoms that connect rigid units impose severe constraints on any rotational degrees of freedom, which must then be cooperative throughout the entire network. Successful efforts to identify cooperative-rotational rigid-unit modes (RUMs) in crystals have employed split-atom harmonic potentials, exhaustive testing of the rotational symmetry modes allowed by group representation theory, and even simple geometric considerations. This article presents a purely algebraic approach to RUM identification wherein the conditions of connectedness are used to construct a linear system of equations in the rotational symmetry-mode amplitudes.

1. Introduction

There is an extensive literature exploring the structural effects of cooperative 'tilting' or 'rotation' of interconnected rigid units within crystalline compounds, most of which is concerned with the case of rigid polyhedral units connected within inorganic compounds or organic–inorganic hybrids. One aim of the work is to determine what happens to the structure, including a possible lowering of symmetry, when cooperative rotations occur. Such rotations are important in the silicates, in which the rotation of SiO_4 tetrahedra plays a role in the structural phase transitions from the high (β) to the low (α) forms in quartz (see, for example, Heaney & Veblen, 1991), tridymite (Pryde & Dove, 1998) and cristobalite (Hatch & Ghose, 1991). In perovskites, ABX_3, the corner-linked BX_6 octahedra form the framework, and the tilting of these octahedra leads to phase transitions from the cubic to an assortment of lower-symmetry structures – this system has received perhaps more attention than the silicate one (Megaw, 1973; Glazer, 1972; Aleksandrov, 1976; Woodward, 1997*a*,*b*; Howard & Stokes, 2005, and references therein). In the event that the BX_6 octahedra are sufficiently large, the cavity may contain an organic entity in place of the single cation A and an organic–inorganic hybrid results. Such is the case for frameworks comprising tin and lead iodides (Stoumpos *et al.*, 2013; Whitfield *et al.*, 2016); notwithstanding the presence of this organic entity, the structures are still largely determined by the tilting of the BX_6 octahedra in the framework. Spinels AB_2O_4 can be viewed as three-dimensional networks of edge-sharing BO_6 octahedra incorporating AO_4 tetrahedra, and as such are

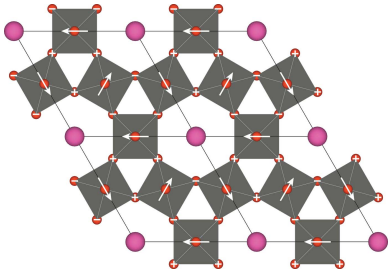

expected to be less flexible than silicates or perovskites; nevertheless tilting of the polyhedra may be possible (Talanov & Shirokov, 2012).[1] In the tungsten bronzes, M_xWO_3, the frameworks are arrangements of corner-linked WO_6 octahedra, and thus are expected to be susceptible to octahedral tilting. Possible tilted structures have been listed in recent works (Smirnov & Saint-Grégoire, 2014; Whittle *et al.*, 2015), but it will be shown here that these lists are incomplete. The present work was motivated in part by shortcomings noticed in that previous work on the bronzes.

The tilting or rotation just described is driven by the usual forces of chemistry. In the perovskites, for example, it is often due to the cavity cation *A* being undersized. This situation can be assessed from ionic radii using the Goldschmidt tolerance factor (Goldschmidt, 1926), or perhaps more reliably from the bond valence calculations available in the computer program *SPuDS* (Lufaso & Woodward, 2001).

The structural phase transitions effected by cooperative rotations are of rather more than esoteric interest. Such transitions lead in the first instance to 'spontaneous strain' (Carpenter *et al.*, 1998); associated with the transition from high to low forms of quartz, for example, there is a non-symmetry-breaking spontaneous strain below the transition, resulting in a volume contraction up to 5%. There are, too, significant anomalies in elastic constants (Carpenter & Salje, 1998) – documented anomalies (*loc. cit.*) include those at the quartz transition, and at the cubic to-tetragonal transitions in $KMnF_3$ and $SrTiO_3$ perovskites. Strains and elastic constants in minerals such as quartz and the perovskites are of considerable importance in the earth sciences, and in particular in seismology. In the case of the ABX_3 perovskites, tilting will lead to a change in the $B-X-B$ bond angle and it is thought (see for example He *et al.*, 2010) this may affect the electronic band structure and the properties – optical, electrical and magnetic – that depend on it. In some layered compounds, such as hexagonal $YMnO_3$, the Aurivillius phase $SrBi_2Ta_2O_9$ and Ruddlesden–Popper $Ca_3Ti_2O_7$, tilting leads to electric polarization (Howard *et al.*, 2013; Benedek *et al.*, 2015): in $YMnO_3$ the tilting of corner-connected MnO_6 octahedra occurs simultaneously with and very probably drives displacement of the Y^{3+} ions, whereas in the Aurivillius or Ruddlesden–Popper phases the combination of tilting around two different axes breaks the centre of symmetry and a polarization perpendicular to both these axes develops. Irrespective of the physical effects of rigid-unit modes (RUMs) we believe it critical that the structures they yield should be understood as a basis for any detailed experimental or theoretical materials investigation.

Although the emphasis of this article will be on the structures resulting from the 'freezing in' of RUMs, it is noted that in the higher-symmetry phases these same cooperative rotations exist as low-frequency or 'soft' modes of vibration (Giddy *et al.*, 1993). In their dynamic manifestation, these RUMs can be observed by inelastic neutron scattering as low-frequency phonons. We cite, as two examples, the classic observation of the soft-mode phonons in perovskite $SrTiO_3$ just above the 110 K cubic to-tetragonal transition (Shirane & Yamada, 1969), and a more recent study of cristobalite showing an enhancement of low-frequency mode(s) in the high-temperature form of cristobalite (Swainson & Dove, 1993). The dynamic versions of RUMs are also implicated in many instances of negative thermal expansion (see the review by Dove & Fang, 2016).

By rigid unit we understand a set of atoms within the crystal structure that we might choose to rotate collectively without altering any of the interatomic distances or angles within the set, such as an organic molecule, macromolecule, molecular complex or inorganic polyhedral unit. The rotational degrees of freedom of an individual rigid unit are determined by the site symmetry of the pivot point around which it rotates. When two or more rigid units share an atom (or two atoms) in common, the resulting need to cooperate in their motions often reduces the overall rotational freedom of the individual rigid units. The determination of the allowed patterns of cooperative rotation is our present focus. In §2 we outline the developed method and the manner in which it is applied, and illustrate the method by detailing applications to an orthorhombic perovskite and to quartz. We then focus on the perovskite system in §3, the hexagonal tungsten bronzes in §4 and the tetragonal tungsten bronzes in §5.

2. The method

2.1. Glossary of abbreviations

RUM (rigid-unit mode). A global pattern of cooperative rigid-unit rotations in a network of interconnected polyhedra. We might have added a 'C' and another 'R' to the front of the abbreviation to emphasize 'cooperative' and 'rotational', but decided not to attempt to replace an abbreviation that's already common in the literature.

SADP (shared-atom displacement parameter). Any vector component of the displacement of an atom shared by multiple rigid units.

SUSA (symmetry-unique shared atom). A shared atom that is also uniquely identified in the input to the present algorithm as being the symmetry-unique representative for all other symmetry-equivalent atoms in the crystal.

SUPA (symmetry-unique pivot atom). A rigid-body pivot atom that is also uniquely identified in the input to the present algorithm as being the symmetry-unique representative for all other symmetry-equivalent pivot atoms in the crystal. It must be connected to at least one shared atom to receive this designation.

DCPA (directly connected pivot atom). For a given symmetry-unique shared atom, this is a pivot atom that is directly connected to or associated with that shared atom, not merely in some symmetry-equivalent position far from the shared atom. A DCPA need not be a SUPA, though it will always be symmetry-equivalent to a SUPA.

[1] In this instance, rotation of one kind of polyhedron, *e.g.* tetrahedron, must be accompanied by distortion of the other.

Irrep (irreducible representation). An irreducible matrix representation of some mathematical symmetry group, specifically of the crystallographic space group of the parent structure. This is a set of matrices (one for each group element) that obey the same multiplication table as the group and which cannot simultaneously be brought to block-diagonal form by any similarity transform. For a given wavevector, a space group has a finite number of irreps, each of which is a sort of 'recipe' for composing symmetry-breaking order parameters.

OPD (order-parameter direction). An abstract direction in the carrier vector space of an irrep.

HTB (hexagonal tungsten bronze) and TTB (tetragonal tungsten bronze). Well known structure types for tungsten oxides of composition M_xWO_3.

2.2. Scope

Each rigid unit in the structure is assigned a pivot site around which the rigid unit rotates if its rotation is permitted. Each pivot site either hosts an actual atom or a dummy atom, where 'dummy' implies an extra atom that has been artificially inserted into the model. We will thus refer to 'pivot' atoms without further qualification. Aside from the pivot atom, all other atoms of a rigid unit are referred to as 'passenger' atoms. In structures that possess interconnected rigid units, two or more rigid units can share the same passenger atom, which we refer to as a 'shared' atom.

The full scope of the present work is quite general. It accommodates non-connected rigid units, clusters of interconnected rigid units, long-range networks (one-dimensional, two-dimensional or three-dimensional) of interconnected rigid units, or combinations of any of these scenarios. It can accommodate multiple types of rigid units and rigid-unit connections. It allows both one-point (*e.g.* polyhedral-corner) sharing and two-point (*e.g.* polyhedral-edge) atom sharing between rigid units; we do not explicitly preclude three-point (*e.g.* polyhedral-face) atom sharing, though this effectively welds the constituent rigid units into larger rigid units, which might prevent any cooperative rigid-unit rotations in some three-dimensional networks. It even allows more than two rigid units to possess a common shared atom.

2.3. Algorithm

The algorithm is laid out herein as an eight-step procedure. The reader might find it helpful to read, alongside this exposition, §2.7, where the execution of these steps in the concrete case of a *Pnma* perovskite can be followed.

Step 1. We start with a parent structure that can be described in terms of one or more rigid units, in addition to any other atoms present that are not contained within rigid units. The parent is the structure for which RUMs are to be identified. Choose a child symmetry group (*i.e.* a subgroup of the symmetry group of the parent) that has sufficiently low symmetry to accommodate any wavevectors and rotational order parameters of interest. There is some art in the selection of the child subgroup. Depending on the problem and our specific intent, we may or may not need a supercell, and may or may not choose the space group to be $P1$ within the selected supercell. We might choose the child symmetry to be only low enough to accommodate a specific order parameter at a specific wavevector. Or it could prove more useful to lower the symmetry far enough to accommodate the most general order parameter permitted by that wavevector or by some set of distinct wavevectors. In essence, the child selected defines the scope of the subsequent analysis, and will enable both primary and secondary rotational order parameters, all of which can be explored simultaneously.

Any rigid unit that is capable of rotation on a specific site of the child structure will be assumed to rotate about a pivot atom that is centrally located within the rigid unit.

If the symmetry of the parent structure already permits rigid-unit rotations, we simply define all of the rotational angles to be zero in the parent. Any rotational *changes* relative to the parent structure will subsequently be accounted as non-zero. When it is possible to do so, we may want to manually reverse any rigid-unit rotations observed in the parent, which could result in a higher symmetry, and then study the rotational parameters of this new high-symmetry parent instead. Choosing a parent that already has non-zero RUMs, when we could do otherwise, will not change the efficacy of the subsequent analysis, though it will generally result in a rotational parameter set that is less elegant and less intuitive.

Step 2. Let index α run over the list of SUSAs that connect rigid units together, and let the αth SUSA be located at $\mathbf{x}_\alpha$. Let the index γ run over the list of SUPAs. Let index β run over the list of pivot atoms that are directly connected to the αth SUSA; we call them DCPAs. All DCPAs must be listed separately, whether or not they are in the SUPA list, and whether or not they are symmetry equivalent to one another. Because there is a distinct β index for each SUSA, we could instead express it as β_α, but avoid doing so in order to keep the notation simple. Let the βth DCPA of the SUSA at $\mathbf{x}_\alpha$ be located at $\mathbf{y}'_{\alpha\beta}$; and let the SUPA to which it is symmetry equivalent be located at $\mathbf{y}_{\alpha\beta}$. Let $\mathbf{d}'_{\alpha\beta}$ and $\mathbf{d}_{\alpha\beta}$ be the vectors that describe the rigid-unit displacements of the pivot atoms located, respectively, at $\mathbf{y}'_{\alpha\beta}$ and $\mathbf{y}_{\alpha\beta}$. Let $\mathbf{r}'_{\alpha\beta}$ and $\mathbf{r}_{\alpha\beta}$ be the vectors[2] that describe the rigid-unit rotations about the pivot atoms located, respectively, at $\mathbf{y}'_{\alpha\beta}$ and $\mathbf{y}_{\alpha\beta}$. And let $\mathbf{P}_{\alpha\beta}$ and $\mathbf{p}_{\alpha\beta}$ be the point and shift components, respectively, of the symmetry operator of the child space group that maps the SUPA at $\mathbf{y}_{\alpha\beta}$ to the DCPA at $\mathbf{y}'_{\alpha\beta}$. Because $\mathbf{y}_{\alpha\beta}$ is the location of a SUPA indexed by γ, we could instead express it as $\mathbf{y}_{\gamma(\alpha\beta)}$, but avoid doing so to keep the notation simple; the same applies to the unprimed quantities $\mathbf{d}_{\alpha\beta}$, $\mathbf{r}_{\alpha\beta}$, $\mathbf{P}_{\alpha\beta}$ and $\mathbf{p}_{\alpha\beta}$.

The structural parameters of the DCPAs are related to those of the corresponding SUPAs according to

$$\begin{aligned}\mathbf{y}'_{\alpha\beta} &= \mathbf{P}_{\alpha\beta}\cdot\mathbf{y}_{\alpha\beta}+\mathbf{p}_{\alpha\beta}\\ \mathbf{d}'_{\alpha\beta} &= \mathbf{P}_{\alpha\beta}\cdot\mathbf{d}_{\alpha\beta}\\ \mathbf{r}'_{\alpha\beta} &= \det(\mathbf{P}_{\alpha\beta})\mathbf{P}_{\alpha\beta}\cdot\mathbf{r}_{\alpha\beta}.\end{aligned}\qquad(1)$$

[2] Throughout this work, vectors are taken to be column vectors.

The inclusion of the determinant factor in the transformation of the rotation vector reflects the fact that rotations are axial vectors.

Step 3. Now we calculate the displacement $\mathbf{u}_\alpha$ of the SUSA at $\mathbf{x}_\alpha$ due to the rotation of the DCPA at $\mathbf{y}'_{\alpha\beta}$. In the limit of small rotation angles, the magnitude of this displacement is simply the product of the rotation angle and the perpendicular separation between the shared atom and the rotation axis, which means that the displacement vector is just the cross product of these rotation and separation vectors. And of course, if the DCPA is displaced as well, the SUSA will follow. The result for $\mathbf{u}_\alpha$ can be expressed in terms of the displacements and rotations of either the DCPA at $\mathbf{y}'_{\alpha\beta}$ or the SUPA at $\mathbf{y}_{\alpha\beta}$:

$$\begin{aligned}\mathbf{u}_\alpha &= B^{-1}\cdot\{(B\cdot\mathbf{r}'_{\alpha\beta})\times[B\cdot(\mathbf{x}_\alpha-\mathbf{y}_{\alpha\beta}\prime)]\}+\mathbf{d}'_{\alpha\beta}\\ &= B^{-1}\cdot(\{B\cdot[\det(\mathbf{P}_{\alpha\beta})\mathbf{P}_{\alpha\beta}\cdot\mathbf{r}_{\alpha\beta}]\}\\ &\quad\times[B\cdot(\mathbf{x}_\alpha-\mathbf{P}_{\alpha\beta}\cdot\mathbf{y}_{\alpha\beta}-\mathbf{p}_{\alpha\beta})])+\mathbf{P}_{\alpha\beta}\cdot\mathbf{d}_{\alpha\beta}.\end{aligned}\tag{2}$$

Here, B is the matrix whose columns are the Cartesian coordinates of the basis vectors of the unit cell. All vector quantities in equation (2) are presented in lattice coordinates rather than Cartesian coordinates. Because the definition of the cross product in a non-Cartesian coordinate system is somewhat complicated, we instead use B to transform vector quantities to Cartesian coordinates prior to taking a cross product, and then use B^{-1} to transform the result back into lattice coordinates. See Appendix *A* for a discussion of the coordinate systems used to describe rotational vectors.

The linearity of equation (2) in the rotational components is a feature key to the development of the present algorithm. By assuming the small rotational-angle limit, we have essentially linearized the RUM-search problem.

Step 4. The set of $N_{\rm pivot}$ SUPAs has $3N_{\rm pivot}$ displacive vector components and $3N_{\rm pivot}$ rotational vector components. From these, collect all of the displacive and rotational vector components that are both free and independent, and place them in a single $N_{\rm free}$-dimensional vector called **S**. By free, we mean that the component is allowed by the child space-group symmetry to be non-zero. By independent, we mean that the component is not dependent by symmetry on another component of the same vector. For example, for a rotation vector of the form $(r_x, r_x, 0)$, only the first component is both free and independent.

The set of $N_{\rm shared}$ SUSAs has $3N_{\rm shared}$ displacive vector components, which we refer to as SADPs. Place all of the SADPs in a single $3N_{\rm shared}$-dimensional vector called **U**. In contrast to **S**, we do not require the components of **U** to be free or independent. Both **S** and **U** should be viewed as containing variable parameters rather than numbers.

Step 5. For each possible pair (α, β), which is a unique combination of a SUSA and a DCPA, apply equation (2) to obtain a linear vector relationship in the components of **U** and **S** with numerical coefficients. The expression for each vector component of $\mathbf{u}_\alpha$ yields a linear equation; there will be three separate equations for each distinct combination of α and β. Let $N_{\rm eqs}$ be the number of equations so generated. All together, this system of equations can be expressed as

$$\mathbf{T}_U\cdot\mathbf{U}=\mathbf{T}_S\cdot\mathbf{S}\tag{3}$$

where $\mathbf{T}_U$ is an $N_{\rm eqs}\times 3N_{\rm shared}$ numerical matrix and $\mathbf{T}_S$ is an $N_{\rm eqs}\times N_{\rm free}$ numerical matrix.

A given row of $\mathbf{T}_U$ contains only one non-zero element (which is equal to '1'), located in the column of the relevant shared-atom displacement component. Because a shared atom is by definition connected to multiple pivot atoms, each of its components must appear in multiple equations, so that a given column of $\mathbf{T}_U$ will always contain more than one '1'; as a result, every unique row of $\mathbf{T}_U$ is duplicated at least once, which structure is essential to the algorithm. Whenever identical rows of $\mathbf{T}_U$ have non-identical counterpart rows in $\mathbf{T}_S$, a shared atom is tied to multiple pivot atoms that attempt to simultaneously move the shared atom in different directions. Together, such rows comprise a constraint that restricts the allowed rotational parameters. To violate such a constraint would be akin to splitting the shared atom into fragments. This is the primary insight that makes our algebraic approach to the RUM-search problem possible!

Step 6. The vector **S** comprises what we call the 'traditional' parameter set for describing the rotations and displacements of the individual rigid units in the structure. We will also use the symmetry-mode parameter set, which consists of order parameters of the irreps of the parent symmetry group. The relationship between the two parameter sets is linear, meaning that each traditional parameter can be expressed as a linear combination of symmetry modes. And in fact, one can always find a complete and orthogonal basis of symmetry modes for the parameter space in question, a well known and quite general result from group representation theory based on Schur's lemma (Bradley & Cracknell, 1972, section 1.3; Stokes, 2006; Campbell *et al.*, 2006). The standard procedure for calculating symmetry modes is to build a reducible representation that describes the action of each parent symmetry element on the traditional parameter set, to decompose it as a direct sum of irreps, and then to use the method of projection (Bradley & Cracknell, 1972, section 2.2) to identify linear combinations of traditional parameters that transform as basis functions of each contributing irrep. The process is straightforward; but in all but the simplest cases, one typically needs computational tools to perform the projection.

Assign a variable amplitude to each relevant rotational and displacive symmetry mode, and collect these parameters into an $N_{\rm free}$-dimensional vector called **A**. If all secondary order parameters are properly included, the conversion from traditional to symmetry-mode coordinates does not change the number of independent parameters; the linear transformation is invertible. We call the square invertible $N_{\rm free}\times N_{\rm free}$ matrix that relates the two parameter sets $\mathbf{T}_A$, so that

$$\mathbf{S}=\mathbf{T}_A\cdot\mathbf{A}.\tag{4}$$

Next, combine equations (3) and (4), and move all terms to the left-hand side of the equation to obtain

$$\mathbf{T}_U \cdot \mathbf{U} - \mathbf{T}_S \cdot \mathbf{T}_A \cdot \mathbf{A} = 0. \quad (5)$$

This equation describes the linear relationship between the set of SADPs and the set of rotational and displacive symmetry modes. Note that an algebraic approach to determining the RUMs of the child structure does not *require* the use of symmetry-mode parameters. We employ symmetry modes because (i) each symmetry mode has a well defined **k** vector in the first Brillouin zone of reciprocal space, (ii) each symmetry mode breaks the symmetry of the parent structure in a characteristic and rather elegant way, and (iii) phase transitions in crystals tend to activate a relatively sparse subset of the available symmetry modes (rotational or otherwise).

Step 7. Place all of the parameters from **U** and **A** into a single $(3N_{\rm shared} + N_{\rm free})$-dimensional vector called $\mathbf{V} = \{\mathbf{U}|\mathbf{A}\}$, such that the SADPs of **U** are positioned before the symmetry-mode parameters of **A**. Then construct an $N_{\rm eqs} \times (3N_{\rm shared} + N_{\rm free})$-dimensional matrix $\mathbf{M} = \{\mathbf{T}_U| - \mathbf{T}_S \cdot \mathbf{T}_A\}$, such that the columns of $\mathbf{T}_U$ are positioned before the columns of $-\mathbf{T}_S \cdot \mathbf{T}_A$. This allows us to rewrite equation (5) as

$$\mathbf{M} \cdot \mathbf{V} = 0. \quad (6)$$

The solution space of this homogeneous system of $N_{\rm eqs}$ linear equations in $3N_{\rm shared} + N_{\rm free}$ parameters will contain all allowed RUMs.

Step 8. Reduce the matrix **M** of coefficients to reduced-row-echelon form, wherein the first non-zero element in each non-zero row is a 1 (referred to as a 'row-leading 1') and each column containing a row-leading 1 has no other non-zero elements. Such a reduction is always possible and leads to a unique result (theorem #1 in Lay, 1997). Call the new matrix $\mathbf{M}_{\rm rre}$, so that we now arrive at

$$\mathbf{M}_{\rm rre} \cdot \mathbf{V} = 0. \quad (7)$$

Because equations (6) and (7) share the same solution space, the simplified form $\mathbf{M}_{\rm rre}$ allows us to quickly identify the independent symmetry modes of the original set of equations and to show how each of the SADPs depends on these independent modes.

Because a SADP always depends on something else (*i.e.* pivot-atom rotational and displacive symmetry-mode parameters), the corresponding column in the $\mathbf{M}_{\rm rre}$ must contain a row-leading 1; if the row-leading 1 is alone (*i.e.* the only non-zero value) on its row, the SADP must from equation (7) be identically zero; otherwise it will depend on the symmetry modes indicated by the columns of the other non-zero elements on its row. Due to our construction of the problem, one SADP cannot depend on other SADPs – this ensures that no row can have non-zero values in more than one SADP column. The columns of the symmetry-mode parameters are more interesting. A symmetry mode whose column contains a row-leading 1 that is also alone in its own row must be identically zero; the shared-atom constraints forbid its activation. A symmetry mode whose column contains a row-leading 1 that is not alone in its own row is not prevented by the shared-atom constraints, but depends on other symmetry modes rather than being independent. A symmetry mode whose column contains non-zero terms other than a row-leading 1 is allowed and also independent, the specific values showing how the mode affects the various other symmetry modes and shared-atom displacements that depend on it.

2.4. Quasi-RUMs

The independent rotational symmetry modes identified using the above algorithm are 'pure' in the sense that an infinitesimal rotation amplitude requires no internal distortions of the affected rigid units.[3] However, the application of a finite rather than infinitesimal amplitude to a pure RUM will inevitably lead to rigid-unit distortions. Though we do not allow the cell parameters to relax in the present work, this would often be true even if we allowed cell-parameter relaxation. Once a distortion-inducing finite-amplitude RUM has already been applied, any attempt to further adjust the amplitude (whether an increase or a decrease) will further change the current rigid-unit geometries. In such a situation, what was once a pure RUM is now inexact, so that attempts to detect it from equations (6)–(7) using the already distorted structure as a starting point will fail. Yet, this inexact RUM is still clearly of interest to us and ought to be detectable by some approximate means. Following other literature (Withers *et al.*, 2002), we will refer to such modes as 'quasi-RUMs'. Some crystalline materials have fundamental geometric constraints such that even their most idealized forms have slightly irregular rigid units, precluding the existence of pure RUMs, but admitting quasi-RUMs. One rather simplistic solution for detecting quasi-RUMs is described in the next subsection.

2.5. Technical details

ISOTROPY is the original software program in what is now referred to as the *ISOTROPY* software suite (http://iso.byu.edu/iso/isotropy.php). The *ISODISTORT* program (Campbell *et al.*, 2006) extends the capabilities of the *ISOTROPY* program to include new order-parameter types, symmetry-mode search types, incommensurate wavevector and symmetry groups, and many output options. Among other things, *ISODISTORT* can be used to fully parameterize a child structure in terms of the symmetry modes of the various irreps of the parent symmetry, using only irreps that actually contribute order parameters to the child structure. The *ISOSUBGROUP* program (Stokes *et al.*, 2016) is a relatively new addition to the *ISOTROPY* suite; it allows one to conveniently list all of the irreps and OPDs of a given parent symmetry group, independent of any specific order-parameter type (*e.g.* displacive, magnetic, rotational *etc.*). All three of these software packages are either used or discussed below.

The ability to compute the symmetry modes of rotational (axial vector) order parameters is a newly implemented feature of *ISODISTORT* that has not been presented in past

[3] By this we mean that any consequent distortion is not linear but of second or higher order in the tilt angle.

literature. The treatment of rotational moments is perfectly analogous to that of magnetic moments, except that static rotations enjoy greater simplicity due to the avoidance of time-reversal operations and magnetic space groups. Upon uploading the parent structure into *ISODISTORT*, one selects the order-parameter types of interest separately for each chemical element; all atoms of a given element type share a selection. Choose displacive (if needed) and rotational order parameters for each type of pivot atom; but do not select anything for non-pivot atoms. If the atoms of a given chemical element include both pivot and non-pivot atoms, one must artificially change the non-pivot atoms to a different element type in the parent structure before uploading it. This ensures that all order parameters belong exclusively to pivot atoms.

The low-symmetry child structure can be generated in *ISODISTORT* using any one of its standard methods. Then leave all symmetry modes at their default-zero amplitudes, and export the child structure to a CIF file. This file contains a standard description of the undistorted child structure, a list of the $N_{\rm free}$ free and independent traditional child-structure parameters comprising the vector **S**, a list of the $N_{\rm free}$ symmetry-mode parameters comprising the vector **A**, and the numerical matrix $\mathbf{T}_A$.

Though the vectors **S** and **A** have been defined to include both the rotational and displacive degrees of freedom of the pivot atoms, it is often the case that pivot-atom displacements are not relevant to the RUMs available to a structure. The high (β) to the low (α) transition of quartz is a notable counterexample, in which tetrahedral SiO_2 rotations and displacements must be activated cooperatively in order for the rotations to occur at all. But for other cases of interest in the present work, such as perovskite and tungsten-bronze tilt systems, pivot-atom displacements proved to be unnecessary (*i.e.* no rotational modes depended on them) during our initial explorations, and were therefore omitted from the analysis presented here (*i.e.* not included in **S** or **A**).

The *Mathematica* programming language and environment was used to prepare the code that constructs equations (1)–(7). This code uses an *ISODISTORT*-generated CIF file containing the symmetry-mode description of the child structure as input.

Mathematica's built-in *RowReduce* function was applied to the matrix **M** in equation (6) to obtain the matrix $\mathbf{M}_{\rm rre}$ in equation (7). Numerical row reduction naturally requires a tolerance in order to distinguish zero and non-zero values. Numbers with absolute values smaller than the tolerance get set to zero at potential pivot[4] positions during the calculation, which accommodates round-off errors and inherent uncertainty in the initial matrix components.

To detect quasi-RUM modes, which do not quite satisfy equations (6)–(7), but which result in a small discrepancy vector $\boldsymbol{\xi} = \mathbf{M} \cdot \mathbf{V}$, one can simply raise the row-reduction tolerance well above the levels normally needed to accommodate round-off errors and input uncertainties. Of course, when the tolerance grows too large, false solutions of no interest may also be detected. When raising the tolerance to include potential quasi-RUMs, one should scrutinize each detected mode to ensure that it is meaningful.

2.6. Mode superposition

For a structure that allows multiple independent RUMs, it is important to appreciate that any arbitrary superposition of independent RUMs is also a valid RUM (still maintaining the assumption of infinitesimal mode amplitudes). To see that this must be true, consider that every equivalent domain of a RUM-generating OPD must also produce a RUM, and that the equivalent domains of even the simplest OPD, taken together, span the carrier space of an irrep. Thus, we can choose N independent basis RUMs to form the basis of an N-dimensional vector space of RUMs. Though one could do otherwise, in principle, we will always choose each basis RUM of the child structure to belong to a specific irrep of the parent rather than allowing a basis RUM to mix contributions from multiple irreps.

A multi-dimensional irrep is capable of contributing a number of independent RUMs less than or equal to its dimensionality. In this case, the basis RUMs will be defined as those corresponding to OPDs with just a single non-zero component. Consider a two-dimensional irrep for which the $(a, 0)$ and $(0, a)$ OPDs each provide one basis RUM to the child. Because the general (a, b) OPD of the same irrep is a linear combination of its two basis OPDs, it will correspond to a RUM with two free parameters.

The OPD (a, a) has multiple non-zero components but only one independent or free parameter. The OPDs (and the corresponding RUMs) having only one free parameter are referred to here as 'simple'. A complete set of independent (and possibly non-orthogonal) RUMs based on simple OPDs do in fact provide an alternative basis for the vector space of all possible RUMs. But in the present context, we will refer to them as 'simple' RUMs so that we can reserve the term 'basis' for the RUMs corresponding to a single non-zero OPD component; it is clear from these definitions that all 'basis' RUMs are 'simple', but that some simple RUMs may not be basis RUMs.

Suppose that the simple (a, a) OPD results in an intermediate subgroup symmetry that is both lower than the parent symmetry and higher than the child symmetry. If this happens and also proves interesting, one can consider redefining the child structure to have this intermediate symmetry, so that the resulting rotational analysis will yield only a single RUM – that arising from the simple (a, a) OPD. The existing literature favours this approach of separately exploring the RUMs available to each intermediate subgroup that can be achieved with an irrep rather than merely identifying the basis RUMs available to the irrep's lowest-possible subgroup – that of the general OPD. And in fact, one often finds that these intermediate subgroups correspond to real phases of a material. The examples described below will illustrate this concept.

[4] The word 'pivot' as used here is a technical term used in row reduction, and does not here refer to the 'pivot atom' in a rigid unit.

2.7. *Pnma* perovskite example

For a simple but interesting example we return to the perovskites. The ideal perovskite is cubic in space group $Pm\bar{3}m$. However, as indicated in our introductory remarks, perovskites are susceptible to symmetry lowering by rotation (tilting) of the BX_6 octahedra (RUMs), and are found most frequently in space group *Pnma* (Lufaso & Woodward, 2001), on a $2^{1/2} \times 2 \times 2^{1/2}$ supercell relative to the cubic parent. The *Pnma* structure involves two different types of BX_6 rotations. As our specific example, we take the well known room-temperature structure of $LaMnO_3$ (Rodríguez-Carvajal *et al.*, 1998). For the parent structure, we used a cubic perovskite with cell parameter a = 4.0 Å. We then generated an undistorted child structure by artificially lowering the symmetry of the parent from cubic to orthorhombic without varying any of the new structural parameters available to the orthorhombic phase. The cell parameters and atomic coordinates for the idealized cubic, the undistorted child, and the experimentally determined structures are listed in Table 1.

The only SUPA is the Mn atom, which is located at Wyckoff site (0, 0, 0); based on the $\bar{1}$ point symmetry of this site, all three components of the Mn-atom rotation vector $\mathbf{r}_{\rm Mn} = (r_{{\rm Mn},x}, r_{{\rm Mn},y}, r_{{\rm Mn},z})$ are permitted to be non-zero. O atoms O1 and O2 are SUSAs. The two Mn pivot atoms connected to shared oxygen O1 are located at $\mathbf{y}'_{\rm O1,1}$ = (0.5, 0, 0.5) and $\mathbf{y}'_{\rm O1,2}$ = (0.5, 0.5, 0.5) and have rotation vectors $\mathbf{r}'_{\rm O1,1} = (-r_{{\rm Mn},x}, -r_{{\rm Mn},y}, r_{{\rm Mn},z})$ and $\mathbf{r}'_{\rm O1,2} = (r_{{\rm Mn},x}, -r_{{\rm Mn},y}, -r_{{\rm Mn},z})$, while the two Mn pivot atoms connected to shared oxygen O2 are located at $\mathbf{y}'_{\rm O2,1}$ = (0, 0, 0) and $\mathbf{y}'_{\rm O2,2}$ = (0.5, 0, 0.5) and have rotation vectors $\mathbf{r}'_{\rm O2,1} = (r_{{\rm Mn},x}, r_{{\rm Mn},y}, r_{{\rm Mn},z})$ and $\mathbf{r}'_{\rm O2,2} = (-r_{{\rm Mn},x}, -r_{{\rm Mn},y}, r_{{\rm Mn},z})$. These rotations were determined by noting that all of the Mn DCPAs are symmetry equivalent to the Mn SUPA at the origin, so that $\mathbf{y}_{\rm O1,1} = \mathbf{y}_{\rm O1,2} = \mathbf{y}_{\rm O2,1} = \mathbf{y}_{\rm O2,2} = (0, 0, 0)$. The corresponding symmetry operators are $\mathbf{P}_{\rm O1,1} = \mathbf{P}_{\rm O2,2} = \bar{x}, \bar{y}, z$, $\mathbf{P}_{\rm O2,1} = x, y, z$ and $\mathbf{P}_{\rm O1,2} = \bar{x}, y, z$, only the last of which has a negative determinant. Applying these operators to $\mathbf{r}_{\rm Mn}$ produces the respective rotations at $\mathbf{y}'_{\rm O1,1}$, $\mathbf{y}'_{\rm O1,2}$, $\mathbf{y}'_{\rm O2,1}$ and $\mathbf{y}'_{\rm O2,2}$.

With two pivot atoms per shared atom, equation (2) yields two equations for each of the six SADPs: $u_{{\rm O1},x} = -2r_{{\rm Mn},z}$, $u_{{\rm O1},y} = 0$, $u_{{\rm O1},z} = -2r_{{\rm Mn},x}$, $u_{{\rm O1},x} = -2r_{{\rm Mn},z}$, $u_{{\rm O1},y} = 0$, $u_{{\rm O1},z} = -2r_{{\rm Mn},x}$, $u_{{\rm O2},x} = 2r_{{\rm Mn},y}$, $u_{{\rm O2},y} = -r_{{\rm Mn},x} + r_{{\rm Mn},z}$, $u_{{\rm O2},z} = -2r_{{\rm Mn},y}$, $u_{{\rm O2},x} = 2r_{{\rm Mn},y}$, $u_{{\rm O2},y} = -r_{{\rm Mn},x} - r_{{\rm Mn},z}$, $u_{{\rm O2},z} = -2r_{{\rm Mn},y}$, where we have employed the parent ($a_{\rm p}$ = 4 Å) and child ($a = c = 2^{1/2}a_{\rm p}$, $b = 2a_{\rm p}$) cell-edge lengths. Recall that the displacements (unitless) and rotations (radians/Å) are both presented in lattice coordinates, so that their relationship involves the child-structure cell parameters a, b and c (see Appendix *A* for more information on rotation-vector components).

Using *ISODISTORT*, we find that there are three rotational symmetry modes that contribute to the allowed traditional rotational degrees of freedom. To each, we assign a variable amplitude: $A_1 = [\frac{1}{2}, \frac{1}{2}, \frac{1}{2}]\,R_4^+(a, -a, 0)$, $A_2 = [0, \frac{1}{2}, 0]\,X_5^+(a, a, 0, 0, 0, 0)$ and $A_3 = [\frac{1}{2}, \frac{1}{2}, 0]\,M_3^+(0, a, 0)$, where the three parts of each name indicate a reciprocal-space **k** vector, an irrep of the parent symmetry group ($Pm\bar{3}m$) at that **k** vector and a specific OPD of that irrep.[5] We place these three rotational symmetry-mode amplitudes together in the vector $\mathbf{A} = (A_1, A_2, A_3)$. The four unnormalized Mn-atom rotation vectors projected for each symmetry mode are as follows:

Mn atom (xyz)	$A_1(R_4^+)$ ($r_x r_y r_z$)	$A_2(X_5^+)$ ($r_x r_y r_z$)	$A_3(M_3^+)$ ($r_x r_y r_z$)
(000)	$(\bar{1}00)$	(001)	(010)
$(0\frac{1}{2}0)$	(100)	$(00\bar{1})$	(010)
$(\frac{1}{2}0\frac{1}{2})$	(100)	(001)	$(0\bar{1}0)$
$(\frac{1}{2}\frac{1}{2}\frac{1}{2})$	$(\bar{1}00)$	$(00\bar{1})$	$(0\bar{1}0)$

From these mode patterns, we can see that $r_{{\rm Mn},x} \propto -A_1$, $r_{{\rm Mn},z} \propto A_2$ and $r_{{\rm Mn},y} \propto A_3$. *ISODISTORT* further normalizes each mode so that the squared amplitude is the sum of the squares of the magnitudes of the affected rotational moments in the supercell. Consider the first (R_4^+) mode, where each of the four Mn moments in the supercell either points parallel or antiparallel to 100 and has magnitude $|B(r_{{\rm Mn},x}, 0, 0)| = a|r_{{\rm Mn},x}|$, so that $A_1^2 = 4a^2|r_{{\rm Mn},x}|^2$ and $r_{{\rm Mn},x} = -(1/2a)A_1 = -(2^{1/2}/16)A_1$. The normalization of the other two modes likewise yields $r_{{\rm Mn},z} = (1/2c)A_2 = (2^{1/2}/16)A_2$ and $r_{{\rm Mn},y} = (1/2b)A_3 = (1/16)A_3$. After defining the **S** and **U** vectors as $S_1 = r_{{\rm Mn},x}$, $S_2 = r_{{\rm Mn},y}$, $S_3 = r_{{\rm Mn},z}$, $U_1 = u_{{\rm O1},x}$, $U_2 = u_{{\rm O1},y}$, $U_3 = u_{{\rm O1},z}$, $U_4 = u_{{\rm O2},x}$, $U_5 = u_{{\rm O2},y}$ and $U_6 = u_{{\rm O2},z}$, we construct the matrices

$$\mathbf{T}_U = \begin{pmatrix} 1 & 0 & 0 & 0 & 0 & 0 \\ 0 & 1 & 0 & 0 & 0 & 0 \\ 0 & 0 & 1 & 0 & 0 & 0 \\ 1 & 0 & 0 & 0 & 0 & 0 \\ 0 & 1 & 0 & 0 & 0 & 0 \\ 0 & 0 & 1 & 0 & 0 & 0 \\ 0 & 0 & 0 & 1 & 0 & 0 \\ 0 & 0 & 0 & 0 & 1 & 0 \\ 0 & 0 & 0 & 0 & 0 & 1 \\ 0 & 0 & 0 & 1 & 0 & 0 \\ 0 & 0 & 0 & 0 & 1 & 0 \\ 0 & 0 & 0 & 0 & 0 & 1 \end{pmatrix}, \mathbf{T}_S = \begin{pmatrix} 0 & 0 & -2 \\ 0 & 0 & 0 \\ -2 & 0 & 0 \\ 0 & 0 & -2 \\ 0 & 0 & 0 \\ -2 & 0 & 0 \\ 0 & 2 & 0 \\ -1 & 0 & 1 \\ 0 & -2 & 0 \\ 0 & 2 & 0 \\ -1 & 0 & -1 \\ 0 & -2 & 0 \end{pmatrix},$$

$$\mathbf{T}_A = \begin{pmatrix} \frac{-2^{1/2}}{16} & 0 & 0 \\ 0 & 0 & \frac{1}{16} \\ 0 & \frac{2^{1/2}}{16} & 0 \end{pmatrix},$$

[5] Because the child symmetry group is a subgroup of index 24 in $Pm\bar{3}m$, there are 24 domains to choose from. The choice of domain affects the forms of the OPDs and the details of the matrices $\mathbf{T}_S$ and $\mathbf{T}_A$, and is arbitrary. When *ISODISTORT*'s 'General Method' (Method 2) is employed, the 'domains' output feature can be used to obtain a list of the OPDs corresponding to each of the domains. The domain employed in the present example was arrived at *via* the decomposition (Method 4) of the child structure presented above.

$$\mathbf{M} = \begin{pmatrix} 1 & 0 & 0 & 0 & 0 & 0 & 0 & 2^{1/2}/8 & 0 \\ 0 & 1 & 0 & 0 & 0 & 0 & 0 & 0 & 0 \\ 0 & 0 & 1 & 0 & 0 & 0 & -2^{1/2}/8 & 0 & 0 \\ 1 & 0 & 0 & 0 & 0 & 0 & 0 & 2^{1/2}/8 & 0 \\ 0 & 1 & 0 & 0 & 0 & 0 & 0 & 0 & 0 \\ 0 & 0 & 1 & 0 & 0 & 0 & -2^{1/2}/8 & 0 & 0 \\ 0 & 0 & 0 & 1 & 0 & 0 & 0 & 0 & -1/8 \\ 0 & 0 & 0 & 0 & 1 & 0 & -2^{1/2}/16 & -2^{1/2}/16 & 0 \\ 0 & 0 & 0 & 0 & 0 & 1 & 0 & 0 & 1/8 \\ 0 & 0 & 0 & 1 & 0 & 0 & 0 & 0 & -1/8 \\ 0 & 0 & 0 & 0 & 1 & 0 & -2^{1/2}/16 & 2^{1/2}/16 & 0 \\ 0 & 0 & 0 & 0 & 0 & 1 & 0 & 0 & 1/8 \end{pmatrix}$$

and

$$\mathbf{M}_{\rm rre} = \begin{pmatrix} 1 & 0 & 0 & 0 & 0 & 0 & 0 & 0 & 0 \\ 0 & 1 & 0 & 0 & 0 & 0 & 0 & 0 & 0 \\ 0 & 0 & 1 & 0 & 0 & 0 & -2^{1/2}/8 & 0 & 0 \\ 0 & 0 & 0 & 1 & 0 & 0 & 0 & 0 & -1/8 \\ 0 & 0 & 0 & 0 & 1 & 0 & -2^{1/2}/16 & 0 & 0 \\ 0 & 0 & 0 & 0 & 0 & 1 & 0 & 0 & 1/8 \\ 0 & 0 & 0 & 0 & 0 & 0 & 0 & 1 & 0 \end{pmatrix}.$$

The matrix **M** has four pairs of identical rows. The duplicate rows are eliminated during row reduction. To identify the critical features of the system of equations, look for non-identical rows in **M** that have their row-leading 1's in the same column; these are rows #8 and #11 in the present example. Adding these two rows and normalizing to the first element yields row #5 of $\mathbf{M}_{\rm rre}$; subtracting one from the other and normalizing yields row #7 of $\mathbf{M}_{\rm rre}$. The all-zero rows of $\mathbf{M}_{\rm rre}$ have been omitted. Solving $\mathbf{M}_{\rm rre} \cdot V = 0$ in equation (7) gives us $u_{\mathrm{O1},x} = 0$, $u_{\mathrm{O1},y} = 0$, $u_{\mathrm{O1},z} = 2^{1/2}/8A_1$, $u_{\mathrm{O2},x} = 1/8A_3$, $u_{\mathrm{O2},y} = 2^{1/2}/16A_1$, $u_{\mathrm{O2},z} = -1/8A_3$ and $A_2 = 0$; these equations comprise a complete description of the allowed RUMs. The only column of $\mathbf{M}_{\rm rre}$ that corresponds to a symmetry mode and also has a row-leading 1 alone on its own row is that corresponding to $A_2(X_5^+)$; thus this mode is prevented; its action splits the shared O1 atom in different directions along the orthorhombic *y* axis.

The $\mathbf{M}_{\rm rre}$ columns corresponding to symmetry modes $A_1(R_4^+)$ and $A_3(M_3^+)$ have non-zero terms other than a row-leading 1, so that these modes are the independent parameters upon which all shared-atom displacements depend. Because there are no dependent symmetry modes, we can say simply that the R_4^+ and M_3^+ modes are the only RUMs available to the child structure. In fact, even if we further lower the child symmetry to space group *P*1, no additional RUMs are found. Acting alone as a single mode, R_4^+ produces the well known $a^0b^-b^-$ octahedral tilt pattern (Glazer notation; Glazer, 1972) with space-group *Imma* (#74), and M_3^+ produces the well known $a^0a^0c^+$ tilt pattern with space group *P*4/*mbm* (#127). Because the superposition of two or more RUMs is also a valid RUM, we are not surprised to find that R_4^+ and M_3^+ can coexist to produce the valid tilt pattern $a^+b^-b^-$ with space group *Pnma* (#62). This is true regardless of the relative sizes of the two mode amplitudes.

Table 1
Structural data for an idealized parent cubic perovskite and a simple $2^{1/2} \times 2 \times 2^{1/2}$ perovskite distortion of $LaMnO_3$ in space group *Pnma* (Rodríguez-Carvajal *et al.*, 1998).

Parent: *Pm*$\bar{3}$*m* (#221), *a* = *b* = *c* = 4.00000 Å
La 4*b* 0.50000 0.50000 0.50000
Mn 4*a* 0.00000 0.00000 0.00000 pivot
O 4*d* 0.50000 0.00000 0.00000 shared
Undistorted child: *Pnma* (#62), *a* = 5.65685, *b* = 8.00000, *c* = 5.65685 Å
La 4*c* 0.00000 0.25000 0.50000
Mn 4*a* 0.00000 0.00000 0.00000 pivot
O1 4*c* 0.50000 0.25000 0.50000 shared
O2 8*d* 0.25000 0.00000 0.25000 shared
Distorted child: *Pnma* (#62): *a* = 5.74731, *b* = 7.69287, *c* = 5.53667 Å
La 4*c* 0.04900 0.25000 0.49220
Mn 4*a* 0.00000 0.00000 0.00000 pivot
O1 4*c* 0.48740 0.25000 0.57450 shared
O2 8*d* 0.30660 0.03840 0.22560 shared

If we choose instead the already distorted structure as the parent, which possesses significant octahedral rotations, we do not expect that any RUMs of interest will be pure. In this case, the matrix **M** is calculated to be

$$\mathbf{M} = \begin{pmatrix} 1 & 0 & 0 & 0 & 0 & 0 & 0 & 0.16376 & 0.03451 \\ 0 & 1 & 0 & 0 & 0 & 0 & -0.02724 & -0.00461 & 0 \\ 0 & 0 & 1 & 0 & 0 & 0 & -0.17646 & 0 & 0.00629 \\ 1 & 0 & 0 & 0 & 0 & 0 & 0 & 0.16376 & 0.03451 \\ 0 & 1 & 0 & 0 & 0 & 0 & 0.02724 & 0.00461 & 0 \\ 0 & 0 & 1 & 0 & 0 & 0 & -0.17646 & 0 & 0.00629 \\ 0 & 0 & 0 & 1 & 0 & 0 & 0 & 0.02515 & -0.10449 \\ 0 & 0 & 0 & 0 & 1 & 0 & -0.08248 & -0.11210 & 0 \\ 0 & 0 & 0 & 0 & 0 & 1 & 0.02710 & 0 & 0.15302 \\ 0 & 0 & 0 & 1 & 0 & 0 & 0 & 0.02515 & -0.12710 \\ 0 & 0 & 0 & 0 & 1 & 0 & -0.10033 & 0.07071 & 0 \\ 0 & 0 & 0 & 0 & 0 & 1 & -0.02710 & 0 & 0.09653 \end{pmatrix}.$$

Using a reasonably small row-reduction tolerance of 0.01, $\mathbf{M}_{\rm rre}$ computes to the identity matrix after all non-zero rows are omitted. In other words, equations (6)–(7) have no non-trivial solution. However, if we increase the tolerance to 0.06, we instead obtain

$$\mathbf{M}_{\rm rre} = \begin{pmatrix} 1 & 0 & 0 & 0 & 0 & 0 & 0 & 0 & 0.03451 \\ 0 & 1 & 0 & 0 & 0 & 0 & -0.02724 & 0 & 0 \\ 0 & 0 & 1 & 0 & 0 & 0 & -0.17646 & 0 & 0.00629 \\ 0 & 0 & 0 & 1 & 0 & 0 & 0 & 0 & -0.10449 \\ 0 & 0 & 0 & 0 & 1 & 0 & -0.08248 & 0 & 0 \\ 0 & 0 & 0 & 0 & 0 & 1 & 0.02710 & 0 & 0.15302 \\ 0 & 0 & 0 & 0 & 0 & 0 & 0 & 1 & 0 \end{pmatrix}.$$

This result is very similar to that of the undistorted case, except for small differences of about 0.035 in the symmetry-mode columns. If the matrix terms smaller than tolerance are eliminated, the resemblance to the undistorted case is clearer, though the remaining terms still exhibit differences of similar magnitude:

$$\mathbf{M}_{\rm rre} = \begin{pmatrix} 1 & 0 & 0 & 0 & 0 & 0 & 0 & 0 & 0 \\ 0 & 1 & 0 & 0 & 0 & 0 & 0 & 0 & 0 \\ 0 & 0 & 1 & 0 & 0 & 0 & -0.17646 & 0 & 0 \\ 0 & 0 & 0 & 1 & 0 & 0 & 0 & 0 & -0.10449 \\ 0 & 0 & 0 & 0 & 1 & 0 & -0.08248 & 0 & 0 \\ 0 & 0 & 0 & 0 & 0 & 1 & 0 & 0 & 0.15302 \\ 0 & 0 & 0 & 0 & 0 & 0 & 0 & 1 & 0 \end{pmatrix}.$$

2.8. Quartz example

Another interesting example is the high (β) to the low (α) phase transition in quartz. Both structures have corner-sharing networks of SiO_2 tetrahedra on the same framework topology, and also the same unit cell (to within lattice strains), which contains three SiO_2 tetrahedra. But the trigonal space group of the α phase ($P3_221$) is a subgroup of the hexagonal space group ($P6_222$) of the β phase, so that α can be viewed as slightly distorted relative to β. The child structure has two more displacive degrees of freedom than the parent. The two extra parameters can be described in terms of a tetrahedral rigid-unit rotation and translation, one of which must depend on the other in order to act cooperatively as a RUM. We list the cell parameters and atomic coordinates of both phases in Table 2.

The two Si pivot atoms connected to the shared oxygen are located at $\mathbf{y}_{O,1} = (0.5, 0, 0.66667)$ and $\mathbf{y}_{O,2} = (0.5, 0.5, 1.0)$. By symmetry, they have rotation vectors $\mathbf{r}_{O,1} = (r_{Si}, 0, 0)$ and $\mathbf{r}_{O,2} = (-r_{Si}, -r_{Si}, 0)$, as well as displacement vectors $\mathbf{d}_{O,1} = (d_{Si}, 0, 0)$ and $\mathbf{d}_{O,2} = (-d_{Si}, -d_{Si}, 0)$. The vector $\mathbf{S} = (r_{Si}, d_{Si})$ contains the two free and independent rotation and displacement vector components. And the vector $\mathbf{A}$ contains the corresponding rotational symmetry mode $A_{1[rot]}$ and displacive symmetry mode $A_{2[dis]}$, both of which are associated with the one-dimensional gamma-point irrep $[0, 0, 0]\Gamma_3$.

With two pivots for the one shared atom, equation (2) yields two equations for each of the three SADPs, for a total of six equations, so that the matrix $\mathbf{T}_U$ has two copies of each row as expected. Because rotational and displacive symmetry modes cannot mix within $\mathbf{T}_A$, it has a block-diagonal form, though the simplicity of having only one mode in each block results in something proportional to a 2×2 identity matrix. The matrix B in this case is not diagonal, but otherwise the computation proceeds just as for the perovskite. The relevant matrices are computed to be

$$\mathbf{T}_U = \begin{pmatrix} 1 & 0 & 0 \\ 0 & 1 & 0 \\ 0 & 0 & 1 \\ 1 & 0 & 0 \\ 0 & 1 & 0 \\ 0 & 0 & 1 \end{pmatrix}, \mathbf{T}_S = \begin{pmatrix} -0.52538 & 1 \\ -1.05075 & 0 \\ 0.82084 & 0 \\ 0.52542 & -1 \\ -0.52542 & -1 \\ 0.82084 & 0 \end{pmatrix},$$

$$\mathbf{T}_A = \begin{pmatrix} 0.11552 & 0 \\ 0 & 0.11552 \end{pmatrix}$$

Table 2
Structural data for α-quartz (Le Page & Donnay, 1976) and β-quartz (Wright & Lehmann, 1981).

For α-quartz, note that we use the modern unit-cell origin of space group #154, which is shifted by (0, 0, 1/6) relative to that of Le Page & Donnay. Observe that adding (0, 0, 1/3) to the atomic positions of the child (α) structure places them near to the corresponding positions in the parent (β) structure.

Parent: $P6_222$ (#180), $a = b = 4.99770$, $c = 5.46010$ Å
Si 3*c* 0.50000 0.00000 0.00000 pivot
O 6*j* 0.41440 0.20720 0.16667 shared
Undistorted child: $P3_221$ (#154), $a = b = 4.99770$, $c = 5.46010$ Å
Si 3*a* 0.50000 0.00000 0.66667 pivot
O 6*c* 0.41440 0.20720 0.83333 shared
Distorted child: $P3_221$ (#154), $a = b = 4.91340$, $c = 5.40520$ Å
Si 3*a* 0.46990 0.00000 0.66667 pivot
O 6*c* 0.41410 0.26810 0.78550 shared

$$\mathbf{M} = \begin{pmatrix} 1 & 0 & 0 & 0.06069 & -0.11552 \\ 0 & 1 & 0 & 0.12138 & 0 \\ 0 & 0 & 1 & -0.09482 & 0 \\ 1 & 0 & 0 & -0.06070 & 0.11552 \\ 0 & 1 & 0 & 0.06070 & 0.11552 \\ 0 & 0 & 1 & -0.09482 & 0 \end{pmatrix}$$

and

$$\mathbf{M}_{\rm rre} = \begin{pmatrix} 1 & 0 & 0 & 0 & 0 \\ 0 & 1 & 0 & 0 & 0.23103 \\ 0 & 0 & 1 & 0 & -0.18048 \\ 0 & 0 & 0 & 1 & -1.90332 \end{pmatrix},$$

where 0.11552 represents $1/(3^{1/2}a)$ and thus depends on the cell parameter a. Because the RUM is pure, a small row-reduction tolerance (2×10^{-5}) is sufficient for detecting it. In reduced-row-echelon form, the last row reveals that the rotational and displacive symmetry modes are both allowed to be non-zero, but that one depends on the other according to the relation $A_{1[rot]} = (1.90332\ \text{rad/Å}) A_{2[dis]}$ or its inverse relation $A_{2[dis]} = (0.52540\ \text{Å/rad}) A_{1[rot]}$, where the displacement amplitude is presented in Å units and the rotation amplitude is presented in radian units. These two degrees of freedom combine to form a single RUM! Because equation (4) implies that $r_{Si} = 0.11552 A_{1[rot]}$ and $d_{Si} = 0.11552 A_{2[dis]}$, we also have $r_{Si} = (1.90332\ \text{rad/Å}) d_{Si}$. The forms of $\mathbf{r}_{O,1}$ and $\mathbf{d}_{O,1}$ above then make it clear that the rotation and displacement have the same sense (either both positive or both negative). Thus, the rigid rotation and displacement of the SiO_2 tetrahedron are parallel rather than antiparallel – they twist and slide in the same direction. The ability of the new algebraic approach to detect rotational–displacive interdependencies was the motivation for highlighting this well known distortion.

3. Perovskites

Howard & Stokes (1998) made use of the computer program *ISOTROPY* to identify structures arising from the cooperative rotation (tilting) of the corner-sharing BX_6 octahedra in ABX_3 perovskites. In this section we show that the algebraic approach developed in this article reproduces their results.

As previously mentioned, the parent cubic perovskite structure has space group $Pm\bar{3}m$ (#221) and has a single B site. The special **k** vectors of the first Brillouin zone of the parent lattice are $\Gamma(0,0,0)$, $X(\frac{1}{2},0,0)$, $M(\frac{1}{2},\frac{1}{2},0)$ and $R(\frac{1}{2},\frac{1}{2},\frac{1}{2})$. The Howard & Stokes study was not extended to **k** vectors on lines or planes of symmetry. Howard & Stokes used *ISOTROPY* to determine that the only irreps at the special points able to contribute rotational distortions at the B sites, with their most general OPDs, were $\Gamma_4^+(a,b,c)$, $R_4^+(a,b,c)$, $X_3^+(a,b,c)$, $X_5^+(a,b,c,d,e,f)$, $M_3^+(a,b,c)$ and $M_5^+(a,b,c,d,e,f)$. The same results can now be found using *ISODISTORT*, first setting the program to consider only rotational distortions at the B site, searching over the special **k** points in turn, then using the drop-down menu available after this search to find and list the contributing irreps.

Howard & Stokes (1998) were able to proceed by manual inspection of the different irreps, thanks to the cubic symmetry of the parent perovskite along with the simplifying fact that the passenger X atoms are located midway between pivot atoms B. This meant that only the directions of tilt axes along with the signs of the tilts needed to be considered. It was concluded that only irreps M_3^+ and R_4^+ would contribute to tilting.

For the algebraic approach, we find using *ISODISTORT* that the lowest-symmetry subgroup that combines all of the rotational B-site order parameters of all of the irreps listed above has space group $P\bar{1}$, a $2\times2\times2$ supercell and a $(0,0,0)$ origin shift relative to the cubic parent. We define this to be the undistorted child structure.

Counting up the dimensions of these rotation-capable irreps, we see that the child structure has $N_{\rm free} = 3+3+3+6+3+6 = 24$ rotational symmetry modes, which is as expected for a triclinic supercell with $N_{\rm pivot} = 8$ B-site SUPAs and three rotational vector components each. The supercell has $N_{\rm shared} = 12$ X-site SUSAs with two DCPAs each. This then yields $N_{\rm eqs} = 3N_{\rm shared}\times 2 = 72$ equations in $3N_{\rm shared} + N_{\rm free} = 60$ parameters. The 72×60 matrices **M** and $\mathbf{M}_{\rm rre}$ are too large to display conveniently for this case. But their consequences are simple. (i) Only the R_4^+ and M_3^+ irreps contribute viable RUMs;[6] shared-atom constraints forbid the others. (ii) These two three-dimensional irreps contribute one order parameter each, and do so with their most general OPD, so that a total of $3+3=6$ basis RUMs define the vector space of all possible RUMs. (iii) None of the allowed rotational symmetry modes depend on other symmetry modes; each rotational symmetry mode is either independent or forbidden.

It can be seen that the algebraic approach identifies exactly the same irreps for rotational distortions as were found by Howard & Stokes (1998). This being the case, the enumeration of the isotropy subgroups and the corresponding possible structures must be the same: there are four tilt patterns arising from irrep M_3^+, six tilt patterns from R_4^+, and 14 from the combined action of M_3^+ and R_4^+. Of these last 14, Howard & Stokes (1998) rejected ten tilt patterns that involved 'in-phase' M_3^+ and 'out-of-phase' R_4^+ tilts around the same axis. In this they were following Glazer (1972), who suggested that tilts in successive layers of the perovskite structure should be equal in magnitude to avoid dimensional mismatch between these layers,[7] even though they might differ in sense. Whether or not we choose to cull the tilt patterns in this way, we see that our new algebraic approach to RUM identification and characterization is consistent with the seminal work of Howard & Stokes.

[6] Note that both of these irreps contributed to the example *Pnma* perovskite considered in §2.

Table 3
Irreps of space group $P6/mmm$ that are capable of contributing rotational W-site order parameters to the HTB child structure (as defined).

In parentheses next to each irrep, the number of contributed order parameters and the irrep dimension are listed. In parentheses next to each **k** vector, the total number of rotational symmetry modes that it contributes is shown. The three irreps that produce RUMs are indicated in bold.

$\Gamma(9)$	$A(9)$	$H(18)$	$K(18)$	$L(27)$	$M(27)$	$\Lambda(54)$	$Q(54)$
$\Gamma_2^+(1,1)$	$A_2^+(1,1)$	$H_2(1,2)$	$K_2(1,2)$	$L_2^+(1,3)$	$M_2^+(1,3)$	$\Lambda_1(1,6)$	$Q_1(1,6)$
$\Gamma_3^+(1,1)$	$\boldsymbol{A_3^+(1,1)}$	$H_3(1,2)$	$K_3(1,2)$	$L_3^+(1,3)$	$M_3^+(1,3)$	$\Lambda_2(3,6)$	$Q_2(3,6)$
$\Gamma_4^+(1,1)$	$A_4^+(1,1)$	$H_4(1,2)$	$K_4(1,2)$	$L_4^+(1,3)$	$M_4^+(1,3)$	$\Lambda_3(3,6)$	$Q_3(3,6)$
$\Gamma_5^+(1,2)$	$A_5^+(1,2)$	$H_5(1,4)$	$K_5(1,4)$	$L_1^-(2,3)$	$M_1^-(2,3)$	$\Lambda_4(2,6)$	$Q_4(2,6)$
$\Gamma_6^+(2,2)$	$\boldsymbol{A_6^+(2,2)}$	$H_6(2,4)$	$K_6(2,4)$	$\boldsymbol{L_2^-(2,3)}$	$M_2^-(2,3)$		
				$L_3^-(1,3)$	$M_3^-(1,3)$		
				$L_4^-(1,3)$	$M_4^-(1,3)$		

4. Hexagonal tungsten bronzes

The ideal hexagonal tungsten bronze (HTB) has stoichiometry $M_{1/3}WO_3$ and space-group symmetry $P6/mmm$ (#191). The structure comprises layers of corner-sharing WO_6 octahedra in both hexagonal and triangular arrangements (Fig. 1); the parent unit cell contains three W atoms on the Wyckoff $3f$ sites.

Here we classify and characterize the RUMs of the corner-sharing WO_6 octahedra of an HTB involving only special **k** vectors. The special **k** vectors of the first Brillouin zone of the parent lattice are $\Gamma(0,0,0)$, $A(0,0,\frac{1}{2})$, $H(\frac{1}{3},\frac{1}{3},\frac{1}{2})$, $K(\frac{1}{3},\frac{1}{3},0)$, $L(\frac{1}{2},0,\frac{1}{2})$ and $M(\frac{1}{2},0,0)$. Of the 60 irreps defined at these **k** vectors it is found, using *ISODISTORT* in the manner described in the previous section, that 42 are capable of contributing rotational W-site order parameters (listed in Table 3). Each irrep contributes with its most general OPD, and some irreps contribute more than one order parameter. Using *ISODISTORT*, we find that the lowest-symmetry subgroup that combines all of the rotational W-site order parameters of all of the listed irreps has space group $P1$, and a lattice basis and origin of $((4,2,0),(-2,2,0),(0,0,2))$ and $(0,0,0)$ relative to the hexagonal parent. We will define this to be our undistorted child structure. We note that this large supercell also allows rotational W-site contributions at two non-special **k** vectors, $\Lambda(\frac{1}{6},\frac{1}{6},0)$ and $Q(\frac{1}{6},\frac{1}{6},\frac{1}{2})$, which are also included in the analysis.

At this point, we refer to the previous contribution on the tilting of the WO_6 octahedra in HTB by Whittle *et al.* (2015).

[7] Such a mismatch would occur only when finite tilts are involved.

Though there were some shortcomings in the work, many of the arguments they presented were valid. For example, Whittle *et al.* argued that tilting around the unique sixfold (z) axis was not possible for three octahedra corner-linked within a triangular arrangement. It followed that the only possible tilting would be around axes in the horizontal (x–y) planes. And any tilting around axes in a horizontal layer implied tilting in the reverse sense around layers above and below. This in turn implied doubling of the c cell parameter, so only those special points of the Brillouin zone with $k_z = \frac{1}{2}$, *viz*. the A, H and L points, would be of concern. We do not make use of this argument in the algebraic approach, but rather will find that the algebraic approach gives results consistent with this conclusion. We note too that combining all of the rotational W-site order parameters at just these three special points leads to the same lowest-symmetry subgroup as found above.

The supercell volume of the child is 24 times larger than that of the parent cell. From Table 3, we see that the total number of rotational symmetry modes available to the child structure is $N_{\rm free} = 9 + 9 + 18 + 18 + 54 + 54 = 216$, which is as expected for a triclinic supercell with $N_{\rm pivot} = 24 \times 3 = 72$ W-site SUPAs and three rotational vector components each. The supercell also has $N_{\rm shared} = 216$ O-site SUSAs with two DCPAs each. This then yields $N_{\rm eqs} = 3N_{\rm shared} \times 2 = 1296$ equations in $3N_{\rm shared} + N_{\rm free} = 864$ parameters. The matrix $\mathbf{M}$ then has dimensions 1296×864.

Table 4
The isotropy subgroups of the parent $P6/mmm$ space-group symmetry of HTB at special $\mathbf{k}$ vectors.

Each entry includes the irrep, OPD, space-group type, supercell basis and origin relative to the parent cell, child/parent primitive cell-volume ratio (s), parent/child symmetry-density ratio or index (i), and the active arms of the star of the $\mathbf{k}$ vector. The star of the A point includes only $k_A = (0, 0, \frac{1}{2})$, while the star of the L point contains $k_{L1} = (\frac{1}{2}, 0, \frac{1}{2})$, $k_{L2} = (0, \frac{1}{2}, \frac{1}{2})$ and $k_{L3} = (\frac{1}{2}, \frac{1}{2}, \frac{1}{2})$. The entries with simple OPDs are indicated in bold.

Irrep	OPD	Space-group type	Basis	Origin	s	i	$\boldsymbol{k}$
$\boldsymbol{A_3^+}$	$\boldsymbol{(a)}$	$\boldsymbol{P6_3/mmc}$ (#194)	$\boldsymbol{(1,0,0)}$, $\boldsymbol{(0,1,0)}$, $\boldsymbol{(0,0,2)}$	$\boldsymbol{(0,0,0)}$	**2**	**2**	$\boldsymbol{k_A}$
$\boldsymbol{A_6^+}$	$\boldsymbol{(a,0)}$	$\boldsymbol{Cmcm}$ (#63)	$\boldsymbol{(1,0,0)}$, $\boldsymbol{(1,2,0)}$, $\boldsymbol{(0,0,2)}$	$\boldsymbol{(0,0,0)}$	**2**	**6**	$\boldsymbol{k_A}$
$\boldsymbol{A_6^+}$	$\boldsymbol{(0,a)}$	$\boldsymbol{Cmcm}$ (#63)	$\boldsymbol{(1,2,0)}$, $\boldsymbol{(-1,0,0)}$, $\boldsymbol{(0,0,2)}$	$\boldsymbol{(0,0,0)}$	**2**	**6**	$\boldsymbol{k_A}$
A_6^+	(a,b)	$P2_1/m$ (#11)	(0, 1, 0), (0, 0, 2), (1, 0, 0)	(0, 0, 0)	2	12	k_A
$\boldsymbol{L_2^-}$	$\boldsymbol{(a,0,0)}$	$\boldsymbol{Immm}$ (#71)	$\boldsymbol{(2,1,0)}$, $\boldsymbol{(0,1,0)}$, $\boldsymbol{(0,0,2)}$	$\boldsymbol{(0,0,\frac{1}{2})}$	**2**	**6**	$\boldsymbol{k_{L1}}$
$\boldsymbol{L_2^-}$	$\boldsymbol{(a,0,a)}$	$\boldsymbol{Fmmm}$ (#69)	$\boldsymbol{(2,0,0)}$, $\boldsymbol{(2,4,0)}$, $\boldsymbol{(0,0,2)}$	$\boldsymbol{(0,0,\frac{1}{2})}$	**4**	**12**	$\boldsymbol{k_{L1}}$, $\boldsymbol{k_{L3}}$
$\boldsymbol{L_2^-}$	$\boldsymbol{(a,a,a)}$	$\boldsymbol{P6/mmm}$ (#191)	$\boldsymbol{(2,0,0)}$, $\boldsymbol{(0,2,0)}$, $\boldsymbol{(0,0,2)}$	$\boldsymbol{(0,0,\frac{1}{2})}$	**8**	**8**	$\boldsymbol{k_{L1}}$, $\boldsymbol{k_{L2}}$, $\boldsymbol{k_{L3}}$
L_2^-	$(a,0,b)$	$C2/m$ (#12)	(2, 0, 0), (0, 0, $\bar{2}$), (0, 2, 0)	(0, 0, $\frac{1}{2}$)	4	24	k_{L1}, k_{L3}
L_2^-	(a,b,a)	$Cmmm$ (#65)	(2, 0, 0), (2, 4, 0), (0, 0, 2)	(0, 0, $\frac{1}{2}$)	8	24	k_{L1}, k_{L2}, k_{L3}
L_2^-	(a,b,c)	$P2/m$ (#10)	(0, 2, 0), (0, 0, 2), (2, 0, 0)	(0, 0, $\frac{1}{2}$)	8	48	k_{L1}, k_{L2}, k_{L3}

When the system of equations is solved *via* the calculation of $\mathbf{M}_{\rm rre}$, we find that only the A_3^+, A_6^+ and L_2^- irreps are capable of producing RUMs. These three irreps, respectively, contribute $1, 2 \times 2 = 4$ and $2 \times 3 = 6$ rotational symmetry modes to the child. But because some modes depend on other modes, the three irreps, respectively, contribute only 1, 2 and 3 basis RUMs, so that the total number of basis RUMs is 6.

Rather than analysing the basis RUMs, which are not especially interesting, we instead focus on the linear combinations of basis RUMs that lead to distinct isotropy subgroups, which were determined using *ISOSUBGROUP*. These ten isotropy subgroups are listed in Table 4, where the six entries with simple OPDs are indicated in the table; each of the corresponding simple RUMs is illustrated and described in the supporting information. Three of these RUMs are also shown below (Figs. 1–3). For a multi-dimensional irrep, the multi-parameter OPDs can be viewed as superpositions of these simple OPDs.

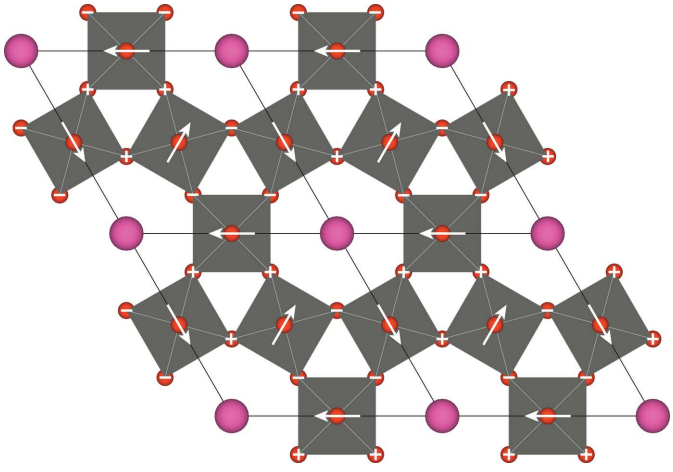

Figure 1
A representation of one layer of the idealized hexagonal tungsten bronze. This shows the WO_6 octahedra, the O ions at the corners of these octahedra and the cations M in the hexagonal tunnels. The arrows are added to indicate the tilt pattern in the structure in $P6_3/mmc$ (irrep A_3^+); they represent the tilt axes as well as the senses and relative magnitudes of the tilts. The 'equatorial' O atoms are marked + or − according to whether the tilting would set them above or below the z = 0 plane. The tilts reverse in sense between one layer and the next.

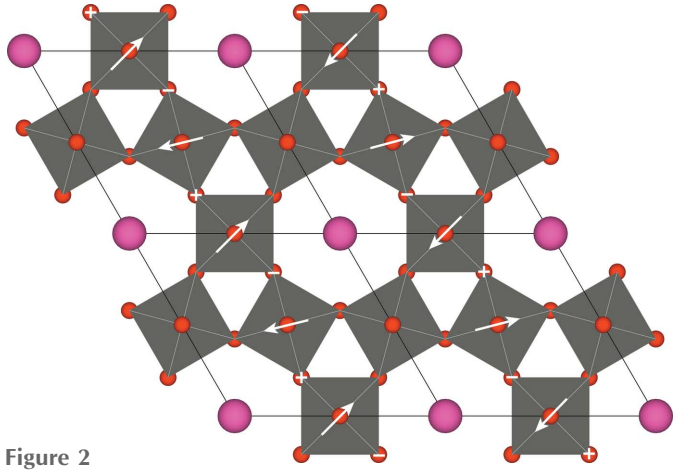

Figure 2
An indication of the tilt pattern in $Immm$, irrep L_2^- with OPD $(a, 0, 0)$. The arrows indicate the tilt pattern as before. Note that some of the WO_6 octahedra remain untilted. It can be seen that the octahedra are untilted and tilted in successive planes of type (010) referred to the parent cell, and this alternation may render the structure unlikely to occur. We are not aware of any experimental observations of this structure.

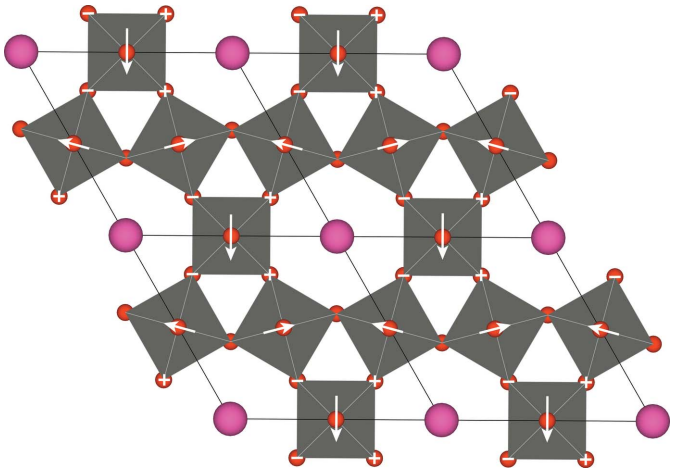

Figure 3
An indication of the tilt pattern in *Cmcm*, irrep A_6^+ with OPD (0, *a*). The arrows indicate the tilt pattern as before. Notice that the tilts are variously around the fourfold and twofold axes of the WO_6 octahedra, and that the magnitudes of the tilts are inversely proportional to the perpendicular distances from passenger O atoms to the tilt axes.

Whittle *et al.* (2015) searched for cooperative tilt patterns in HTB by manual inspection of tilted structures deriving from irreps at the *A*, *H* and *L* points, but this proved a challenging task. They found the structure in $P6_3/mmc$ derived from irrep A_3^+, with tilts as indicated in Fig. 1, and then noted a literature report of this tilted structure in $Cs_{0.29}WO_3$ (Prinz *et al.*, 1992), albeit in a symmetry lowered to space group $P6_322$ by the displacement of the W atoms from the centres of the WO_6 octahedra. They also found the structure in $P6/mmm$ from irrep L_2^- with OPD (*a*, *a*, *a*). However they missed the other structures, some such as that in *Immm* from irrep L_2^- with OPD (*a*, 0, 0), Fig. 2, because they overlooked the possibility that some octahedra could remain untilted, and others such as that in *Cmcm* from irrep A_6^+ with OPD (0, *a*), Fig. 3, because they did not envisage structures with tilts around different axes of the octahedra. On the other hand, they found a pattern of tilting from irrep R_3 on the *R*-line of symmetry at $\mathbf{k} = \frac{1}{4}, 0, \frac{1}{4}$ in space group $P6/mmm$ on a $4 \times 4 \times 2$ supercell; this was not found in the present analysis because the cell chosen for the child structure (as described above) was too small to accommodate it. Further study of RUMs at non-special **k** vectors could be productive.

Because all of the detected RUMs are pure, a very small row-reduction tolerance of 10^{-7} is sufficient for detecting them. We note that false modes begin to appear in the analysis at larger tolerances; in this case at tolerances above 10^{-2}.

5. Tetragonal tungsten bronzes

We also examine the RUMs of the corner-sharing WO_6 octahedra of the tetragonal tungsten bronzes (TTB) involving only special **k** vectors. The structure again comprises layers of corner-linked WO_6 octahedra, but each layer now incorporates triangular, square and pentagonal arrangements of these octahedra (Fig. 4). The stoichiometry would be $M_{0.4}WO_3$ if the pentagonal sites were fully occupied but the tetragonal sites

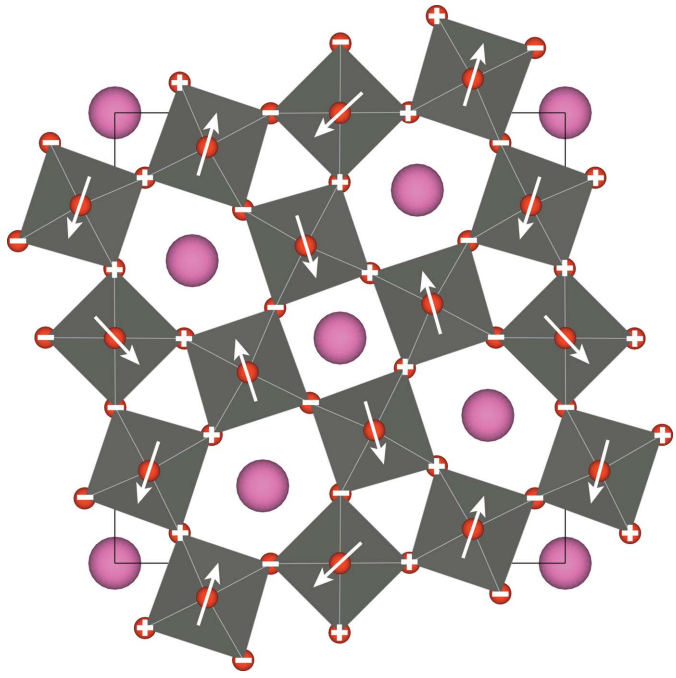

Figure 4
A representation of one layer of a tetragonal tungsten bronze. Notice that the corner-linked WO_6 octahedra show connections in triangular, square and pentagonal arrangements. The cations *M* can reside in the pentagonal and square tunnels. The arrows are added to indicate the tilt pattern in the structure in *Pnma*, irrep Z_5^+ with OPD (*a*, *a*).

empty, and $M_{0.6}WO_3$ if both pentagonal and tetragonal sites were fully occupied; in practice the stoichiometry is variable.[8] It is not possible to construct the structure from identical regular corner-connected octahedra (Whittle *et al.*, 2015), so no idealized structure can be conceived. Instead we take as parent the experimentally determined structure of $Cs_{0.43}WO_3$ (Wachsmann & Jacobs, 1995). The parent then has space-group symmetry $P4/mbm$ (#127) and contains two symmetry-unique W atoms (W1 on the 2*d* Wyckoff site and W2 on the 8*i* Wyckoff site) which yield a total of ten W atoms in the unit cell.

The special **k** vectors of the first Brillouin zone of the parent lattice are $\Gamma(0, 0, 0)$, $M(\frac{1}{2}, \frac{1}{2}, 0)$, $Z(0, 0, \frac{1}{2})$, $X(0, \frac{1}{2}, 0)$, $R(\frac{1}{2}, 0, \frac{1}{2})$ and $A(\frac{1}{2}, \frac{1}{2}, \frac{1}{2})$. All of the 32 irreps defined at these **k** vectors are capable of contributing rotational W-site order parameters (listed in Table 5). Each irrep contributes with its most general OPD, and some irreps contribute more than one order parameter. Using *ISODISTORT*, we find that the lowest-symmetry subgroup that combines all of the rotational W-site order parameters of all of the irreps of all of these special **k** vectors has space group $P1$, and a lattice basis and origin of ((2, 0, 0), (0, 2, 0), (0, 0, 2)) and (0, 0, 0) relative to the tetragonal parent. We will define this to be our undistorted child structure.

Again, it could be argued that only those special points of the Brillouin zone with $k_z = \frac{1}{2}$, *viz.* the *Z*, *A* and *R* points, are of concern. But again, one does not need to make use of this argument in the algebraic approach, but rather will see this

[8] If the triangular sites are also occupied, we have a 'stuffed' tetragonal tungsten bronze.

Table 5
Irreps of space group *P*4/*mbm* that are capable of contributing rotational W-site order parameters to the TTB child structure (as defined).

In parentheses next to each irrep, the number of contributed order parameters and the irrep dimension are listed. In parentheses next to each **k** vector, the total number of rotational symmetry modes that it contributes is listed. The three irreps that produce RUMs are indicated in bold.

$\Gamma(30)$	$M(30)$	$Z(30)$	$A(30)$
$\Gamma_1^+(1,1)$	$M_1^+M_4^+(2,2)$	$Z_1^+(1,1)$	$A_1^+A_4^+(2,2)$
$\Gamma_2^+(2,1)$	$M_2^+M_3^+(2,2)$	$Z_2^+(2,1)$	$A_2^+A_3^+(2,2)$
$\Gamma_3^+(2,1)$	$M_5^+(2,2)$	$Z_3^+(2,1)$	$A_5^+(2,2)$
$\Gamma_4^+(1,1)$	$M_1^-M_4^-(2,2)$	$Z_4^+(1,1)$	$A_1^-A_4^-(2,2)$
$\Gamma_5^+(6,2)$	$M_2^-M_3^-(1,2)$	$\boldsymbol{Z_5^+(6,2)}$	$A_2^-A_3^-(1,2)$
$\Gamma_1^-(2,1)$	$M_5^-(6,2)$	$Z_1^-(2,1)$	$\boldsymbol{A_5^-(6,2)}$
$\Gamma_2^-(2,1)$		$Z_2^-(2,1)$	
$\Gamma_3^-(2,1)$	$X(60)$	$Z_3^-(2,1)$	$R(60)$
$\Gamma_4^-(2,1)$	$X_1(10,4)$	$Z_4^-(2,1)$	$\boldsymbol{R_1(10,4)}$
$\Gamma_5^-(2,2)$	$X_2(5,4)$	$Z_5^-(2,2)$	$R_2(5,4)$

result confirmed as the algebraic approach yields RUMs at these special points only.

The supercell volume of the child is eight times larger than that of the parent cell. From Table 5, we see that the total number of rotational symmetry modes available to the child structure is $N_{\rm free} = 30 + 30 + 30 + 60 + 60 + 30 = 240$, which is as expected for a triclinic supercell with $N_{\rm pivot} = (2 + 8) \times 8 = 80$ W-site SUPAs with three rotational vector components each. The supercell also has $N_{\rm shared} = 240$ O-site SUSAs with two DCPAs each. This then yields $N_{\rm eqs} = 3N_{\rm shared} \times 2 = 1440$ equations in $3N_{\rm shared} + N_{\rm free} = 960$ parameters. The matrix **M** then has dimensions 1440×960.

When the system of equations is solved *via* the calculation of $\mathbf{M}_{\rm irre}$, we find that only Z_5^+ and A_5^- irreps are capable of producing pure RUMs. We further find that the R_1 irrep contributes quasi-RUMs requiring only small octahedral distortions, which we include in all subsequent discussion; their existence reflects the inherent complexity of the octahedral network in the parent structure.

Remarkably, in each case that an irrep contributes multiple order parameters, only one order parameter from that irrep turns out to be independent. Thus, though these three irreps, respectively, contribute a total of $2 \times 6 + 2 \times 6 + 4 \times 10 = 64$ rotational symmetry modes to the child, they, respectively, contribute only $2 + 2 + 4 = 8$ basis RUMs.

Once again, rather than analysing the basis RUMs, we instead focus on the linear combinations of basis RUMs that lead to distinct isotropy subgroups, which were determined using *ISOSUBGROUP*. These 15 isotropy subgroups are listed in Table 6, where the eight entries with simple OPDs are indicated by bold cells; each of the corresponding simple RUMs is illustrated and described in the supporting information.

Whittle *et al.* (2015) conducted a manual search for cooperative tilt patterns in TTB deriving from irreps at *Z*, *A* and *R* points, but with limited success. The only acceptable tilt pattern they identified at special **k** vectors was that in space group $I4/m$ corresponding to irrep A_5^- with OPD $(a, 0)$, as per the entry in Table 6. Smirnov & Saint-Grégoire (2014) enjoyed greater success using a lattice dynamics approach to the problem – they found all the structures with simple OPDs (bold cells in Table 6) apart from that in *Fmmm* (#69) and that in $I4/m$ (#87) on a $2 \times 2 \times 2$ cell.

Whittle *et al.* (2015) found another acceptable tilt pattern at $\mathbf{k} = (\frac{1}{4}, \frac{1}{4}, \frac{1}{2})$, on the *S*-line of symmetry: irrep S_3, OPD $(0, a, 0, 0)$, space group *Cmcm* (#63), basis (0, 0, 2), (2, 2, 0), (−1, 1, 0), origin $(\frac{1}{2}, \frac{1}{2}, \frac{1}{2})$. This tilt pattern does not appear in the present analysis because the child cell used here is too small to have $(\frac{1}{4}, \frac{1}{4}, \frac{1}{2})$ in its reciprocal lattice. An additional doubling of the unit cell in the parent *a*–*b* plane would be sufficient to include this **k** vector. As mentioned earlier for HTB, it may be productive to search for additional TTB RUMs at non-special **k** vectors.

For the algebraic approach presented in this section we took the experimentally determined structure of $Cs_{0.43}WO_3$ (Wachsmann & Jacobs, 1995) as the parent structure. Similar structures have been reported for the tungsten bronzes by a number of authors (Magnéli, 1949; Kihlborg & Klug, 1973; Takusagawa & Jacobson, 1976; Debnath *et al.*, 2009). Since our interest here is in octahedral tilting, we focus on studies reporting a doubling of the *c* parameter (see the argument concerning octahedra linked around a triangle, or the entries in Table 6). Takusagawa & Jacobson (1976) in their study of Na_x-TTBs (x = 0.33, 0.48) reported that the O ions were disordered, attributed this to WO_6 octahedral tilting, and suggested that the ordered structure might be properly described on a $2^{1/2}a \times 2^{1/2}a \times 2c$ cell. A similar superstructure had been observed earlier (Steadman, 1972) in the Sn_x-TTBs at $x = 0.11$ and $x = 0.25$. However in neither case was a space group suggested. This $2^{1/2}a \times 2^{1/2}a \times 2c$ superstructure was reported again in a more detailed study of $Sn_{0.30}$-TTB by Goreaud *et al.* (1980), who gave the space group as *I*4/*m*.

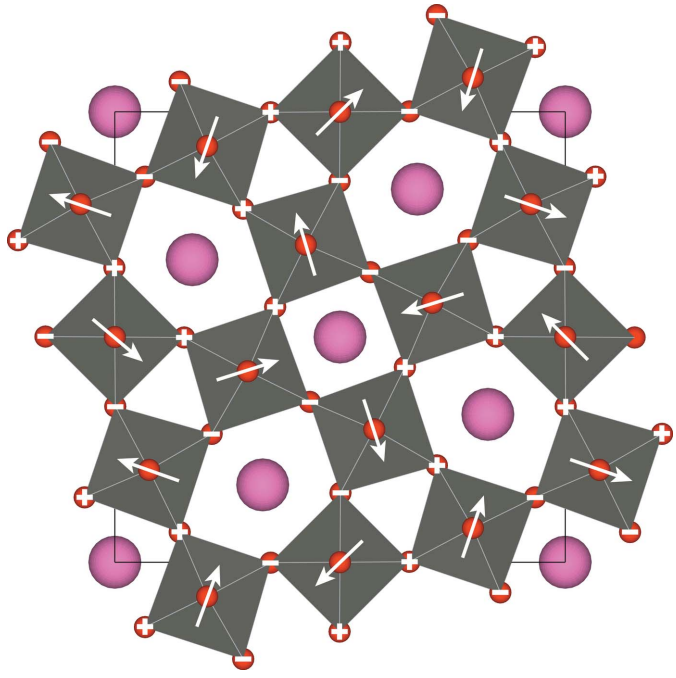

Figure 5
An indication of the tilt pattern in *I*4/*m*, irrep A_5^- with OPD $(a, 0)$. The arrows indicate the tilt pattern as before.

Table 6
The isotropy subgroups of the parent *P*4/*mbm* space-group symmetry of TTB at special **k** vectors.

Each entry includes the irrep, OPD, space-group type, supercell basis and origin relative to the parent cell, child/parent primitive cell-volume ratio (*s*), parent/child symmetry-density ratio (*i*) and the active arms of the star of the **k** vector. The star of the *A* point includes only $k_A = (\frac{1}{2}, \frac{1}{2}, \frac{1}{2})$ and the star of the *Z* point includes only $k_Z = (0, 0, \frac{1}{2})$, while the star of the *R* point contains both $k_{R1} = (\frac{1}{2}, 0, \frac{1}{2})$ and $k_{R2} = (0, \frac{1}{2}, \frac{1}{2})$. The entries with simple OPDs are indicated in bold.

Irrep	OPD	Space-group type	Basis	Origin	*s*	*i*	**k**
$\boldsymbol{Z_5^+}$	$(\boldsymbol{a}, \boldsymbol{0})$	***Cmcm*** (#63)	**(1, 1, 0), (−1, 1, 0), (0, 0, 2)**	$(\boldsymbol{0}, \boldsymbol{\frac{1}{2}}, \boldsymbol{0})$	**2**	**4**	$\boldsymbol{k_A}$
$\boldsymbol{Z_5^+}$	$(\boldsymbol{a}, \boldsymbol{a})$	***Pnma*** (#62)	**(1, 0, 0), (0, 0, 2), (0, −1, 0)**	**(0, 0, 0)**	**2**	**4**	$\boldsymbol{k_A}$
Z_5^+	(a, b)	$P2_1/m$ (#11)	(0, 1, 0), (0, 0, 2), (1, 0, 0)	(0, 0, 0)	2	8	k_A
$\boldsymbol{A_5^-}$	$(\boldsymbol{a}, \boldsymbol{0})$	***I4/m*** (#87)	**(1, 1, 0), (−1, 1, 0), (0, 0, 2)**	$(\boldsymbol{0}, \boldsymbol{0}, \boldsymbol{\frac{1}{2}})$	**2**	**4**	$\boldsymbol{k_Z}$
$\boldsymbol{A_5^-}$	$(\boldsymbol{a}, \boldsymbol{a})$	***Imma*** (#74)	**(0, 0, 2), (1, −1, 0), (1, 1, 0)**	$(\boldsymbol{0}, \boldsymbol{0}, \boldsymbol{\frac{1}{2}})$	**2**	**4**	$\boldsymbol{k_Z}$
A_5^-	(a, b)	$C2/m$ (#12)	(0, 2, 0), (0, 0, 2), (1, −1, 0)	$(0, 0, \frac{1}{2})$	2	8	k_Z
$\boldsymbol{R_1}$	$(\boldsymbol{0}, \boldsymbol{0}, \boldsymbol{a}, \boldsymbol{-a})$	***C2/m*** (#12)	**(2, 0, 0), (0, 0, 2), (0, −1, 0)**	$(\boldsymbol{\frac{1}{2}}, \boldsymbol{0}, \boldsymbol{\frac{1}{2}})$	**2**	**8**	$\boldsymbol{k_{R1}}$
$\boldsymbol{R_1}$	$(\boldsymbol{a}, \boldsymbol{-a}, \boldsymbol{-a}, \boldsymbol{a})$	***Fmmm*** (#69)	**(2, 2, 0), (−2, 2, 0), (0, 0, 2)**	$(\boldsymbol{\frac{1}{2}}, \boldsymbol{0}, \boldsymbol{\frac{1}{2}})$	**4**	**8**	$\boldsymbol{k_{R1}}, \boldsymbol{k_{R2}}$
$\boldsymbol{R_1}$	$(\boldsymbol{0}, \boldsymbol{0}, \boldsymbol{a}, \boldsymbol{0})$	***Cmc2₁*** (#36)	**(0, 0, 2), (2, 0, 0), (0, 1, 0)**	$(\boldsymbol{\frac{3}{4}}, \boldsymbol{0}, \boldsymbol{\frac{1}{2}})$	**2**	**8**	$\boldsymbol{k_{R1}}$
$\boldsymbol{R_1}$	$(\boldsymbol{a}, \boldsymbol{a}, \boldsymbol{-a}, \boldsymbol{a})$	***I4/m*** (#87)	**(2, 0, 0), (0, 2, 0), (0, 0, 2)**	$(\boldsymbol{\frac{1}{2}}, \boldsymbol{\frac{1}{2}}, \boldsymbol{\frac{1}{2}})$	**4**	**8**	$\boldsymbol{k_{R1}}, \boldsymbol{k_{R2}}$
R_1	$(a, -a, b, -b)$	$C2/m$ (#12)	(−2, 2, 0), (0, 0, 2), (2, 0, 0)	$(\frac{1}{2}, 0, \frac{1}{2})$	4	16	k_{R1}, k_{R2}
R_1	$(0, 0, a, b)$	Cm (#8)	(2, 0, 0), (0, 0, 2), (0, −1, 0)	$(0, 0, \frac{1}{2})$	2	16	k_{R1}
R_1	$(a, a, b, -b)$	$C2/m$ (#12)	(−2, 2, 0), (0, 0, 2), (2, 0, 0)	$(\frac{1}{2}, \frac{1}{2}, \frac{1}{2})$	4	16	k_{R1}, k_{R2}
R_1	$(a, b, -a, -b)$	$Fmm2$ (#42)	(0, 0, 2), (2, 2, 0), (−2, 2, 0)	$(0, \frac{1}{2}, \frac{1}{2})$	4	16	k_{R1}, k_{R2}
R_1	(a, b, c, d)	Cm (#8)	(−2, 2, 0), (0, 0, 2), (2, 0, 0)	$(0, 0, \frac{1}{2})$	4	32	k_{R1}, k_{R2}

These authors presented a model for the octahedral tilting in the superstructure, inferred mainly from the disorder found in the substructure, but entirely consistent with what we find in this work (Table 6, Fig. 5). Superstructures have also been reported in studies of Pb_x-TTBs (Triantafyllou *et al.*, 1997; Haydon & Jefferson, 2002). These superstructures have not been directly discernible in X-ray diffraction data but have been observed using electron diffraction techniques. Triantafyllou *et al.* (1997) reported evidence for a modulated structure in $Pb_{0.26}WO_3$, based on the $2^{1/2}a \times 2^{1/2}a \times 2c$ superstructure in *I*4/*m*. They depict a structure showing tilting of the WO_6 octahedra centred on the Wyckoff *d* sites in the manner of Fig. 5, but, strangely, they do not show tilting of the other octahedra. Haydon & Jefferson (2002) reported for $Pb_{0.175}WO_3$ a larger supercell (see discussion in Whittle *et al.*, 2015); interestingly, they found this supercell to be largely independent of Pb content, which was taken to indicate it arises from a distortion of the framework of corner-linked octahedra rather than ordering of the Pb ions within the pentagonal tunnels.

There has been considerable interest in non-centrosymmetric versions of the TTB structures as are found, for example, among the niobates and tantalates, for their potential as piezoelectrics, ferroelectrics and in optical device applications (Ainger *et al.*, 1970; Neurgaonkar *et al.*, 1992; Chi *et al.*, 2004). First, we note that the parent TTB in *P*4/*mbm* can be polarized along its *z* axis due to the displacement of ions along the same axis under the action of irrep Γ_3^-, or it can be polarized in the *x*–*y* plane due to displacement of ions in this plane under the action of irrep Γ_5^-. The effect of Γ_3^- on the parent in *P*4/*mbm* is to lower its symmetry to (tetragonal) *P*4*bm* (#100), while the effect of Γ_5^- is to lower the symmetry to orthorhombic in space groups $Pmc2_1$ (#26), *Amm*2 (#38), or to monoclinic in *Pm* (#6). These results can be obtained using *ISOSUBGROUP*, which also shows that the *A*-centred structure is described on a $c \times 2^{1/2}a \times 2^{1/2}a$ cell. As before, our interest is not so much in these basic structures but rather in any variants showing a doubling of the *c* parameter that might be attributed to octahedral tilting. Doubling of the *c* parameter was reported in a number of early studies (Francombe & Lewis, 1958; Subbarao *et al.*, 1960; Bobb *et al.*, 1969; Jamieson *et al.*, 1969); Jamieson *et al.* (1968) found evidence for oxygen disorder, possibly indicative of unresolved octahedral tilting, while in a study of $Ba_{4.13}Na_{1.74}Nb_{10}O_{30}$ (BNN) the same authors (Jamieson *et al.*, 1969) showed in their Fig. 3 how distorted (sheared) octahedra could stack to cause such a doubling. It is our view that octahedral tilting would be a more likely occurrence [Labbé *et al.* (1989) have expressed a similar opinion].[9] There are reports in the literature of structures with polarization along the *z* axis (irrep Γ_3^-) showing 'weak' orthorhombic distortion; in some instances, the orthorhombic distortion sets in after (*i.e.* at lower temperature than) the paraelectric to ferroelectric transition. This weak orthorhombic distortion is almost invariably accompanied by doubling of the *c* parameter (Jamieson *et al.*, 1969; Neurgaonkar *et al.*, 1992) and it is our contention here that such distortion is simply the result of octahedral tilting. As a specific example, Whittle *et al.* (2018) carried out a study of $Sr_3TiNb_4O_{15}$ (STN) and found the structure to be in space group $Pna2_1$ (#33) on an $a \times a \times 2c$ cell. This structure evidently shows (weak) orthorhombic distortion and a doubling of the *c* parameter; according to *ISOSUBGROUP*, it can arise from a combination of *z*-axis displacements associated with irrep Γ_3^- and octahedral tilting associated with irrep Z_5^+. Other, larger, superstructures have been mentioned elsewhere (Whittle *et al.*, 2015).

For the A_5^- and Z_5^+ RUMs, which were pure, an exceedingly small row-reduction tolerance of 10^{-15} was sufficient for detection. And, as in the case of the HTB analysis, false modes began to arise in the TTB analysis at tolerances above 10^{-2}. The quasi-RUM R_1 modes, however, were only detected when the tolerance was raised to 0.10, by which point the false modes had become excessive. To improve the sensitivity to quasi-RUMs, without introducing false modes, we employed alternative row-reduction tools and strategies, which will be described in a future work.

[9] Jamieson *et al.* (1969) indicated that the BNN structure was based on a $2^{1/2}a \times 2^{1/2}a \times c$ subcell in space group *Cmm*2. Such a subcell would be found in a structure in $Cmc2_1$ on a $2^{1/2}a \times 2^{1/2}a \times 2c$ cell, which in turn could be obtained by introducing *z*-axis polarization (Γ_3^-) into the *Cmcm* structure shown in Table 6; the same subcell could equally be found in a structure in *Ima*2 on a $2^{1/2}a \times 2^{1/2}a \times 2c$ cell obtainable by incorporating *z*-axis polarization into the *Imma* structure of Table 6 (all checked using *ISOSUBGROUP*). There are reports of *Ima*2 structures in the literature (Levin *et al.*, 2006; Stennett *et al.*, 2007).

6. Discussion and conclusions

Two key insights enabled the development of this algebraic method for detecting cooperative rotational rigid units (RUMs) in networks of interconnected rigid units. The first was the realization that the geometric equations of shared-atom motion [equation (2)] in the small rotation-angle limit would be linear, which would enable the construction of a homogeneous linear system of equations. The second key was the separate application of equation (2) to each of the pivot atoms attached to a given shared atom; any incompatibilities amongst these pivot equations are precisely the geometric constraints that cause some modes to be rejected as uncooperative. Another very important but non-critical facet of the new algorithm is the use of rotational (and displacive) symmetry modes to parameterize the child structure's tilt system; this naturally groups the basis RUMs of a system according to wavevector and RUM-capable irrep.

Because each RUM is a solution of a homogeneous system of equations, the superposition of two or more RUMs is also a RUM. In fact, the set of all possible RUMs of a given tilt system comprise a vector space, where the subspace associated with a single instance of a given irrep possesses one basis RUM for each component of the OPD. For a given parent structure and a given multi-dimensional irrep of the parent symmetry, if any OPD component of the irrep is capable of contributing a RUM, then every linear combination of OPD components of the irrep is also capable of contributing a RUM. This was a point not appreciated in past RUM-search efforts on the tungsten bronzes, which excluded some of the OPDs of a RUM-capable irrep. And in general, any RUM can be uniquely decomposed into contributions from the OPD components of the various instances of the RUM-capable irreps, which contributions can be viewed as distinct basis RUMs.

It is also worth noting that if an irrep cannot contribute RUMs to the child structure on its own, it cannot contribute RUMs in conjunction with other irreps; one need not worry that two or more RUM-incapable irreps might somehow work together to produce a RUM. When searching for quasi-RUMs in the perovskite system at non-special wavevectors, with a substantially large row-reduction tolerance, we occasionally saw such modes arise in our output, though in each instance they proved to be spurious.

We anticipate that the present algebraic RUM-search algorithm will eventually be made publicly available as part of the *ISOTROPY* software suite, and that it will complement existing RUM-search tools like *CRUSH* (Hammonds *et al.*, 1994), which simulate classical ball-spring vibrational spectra. In our view, the algebraic approach is the zero-frequency limit of the vibrational spectra approach, and should yield identical results for pure modes, at least in principle. Quasi-RUM modes, which should have non-zero vibration frequencies, can still be detected using the algebraic approach *via* a sufficiently large row-reduction tolerance. The new approach can simultaneously treat all of the wavevectors and rotational order parameters consistent with a given child subgroup, though one can also choose to treat a single wavevector individually by choosing the child sublattice specifically to accommodate this wavevector and simply deleting the columns of matrix M corresponding to any other wavevectors compatible with the child sublattice prior to row reduction.

In this work we have defined a 'pure' mode as an exact solution of the linearized (*i.e.* small-angle) geometric constraint problem. There has been some interest in the literature in whether rigid units can be undistorted at larger rotation angles if lattice parameter relaxation is allowed; among the 15 perovskite structures given by Howard & Stokes (1998), there is only one structure in which undistorted octahedra cannot be accommodated. Indeed, in their structure prediction package for perovskites, *SPuDS*, Lufaso & Woodward (2001) make the assumption that octahedra remain undistorted at larger rotation angles. It may be that in other systems, such as the tungsten bronzes, RUMs that remain cooperative at large rotation angles are relatively rare. A valuable extension of the present work would be a method of detecting whether a given small-angle pure mode is also a large-angle pure mode.

In summary, we have developed a new approach to the analysis of cooperative rotations in networks of interconnected rigid units wherein the geometric constraints of connectedness reduce, in the small rotation-angle limit, to a homogeneous linear system of equations. We further parameterize the cooperative rotations in terms of symmetry modes associated with the irreducible representations (irreps) of the parent space group. For a given parent structure, this algebraic approach yields a complete list of the geometrically possible cooperative-rotational rigid-unit modes (RUMs), from which potential structures can be deduced. The algebraic approach is generally applicable, even when the interconnected subnetwork is of low dimensionality, when the number of pivots connected to a given shared atom is greater than two, or when there are multiple types of rigid units. It is noted however that some geometrically possible RUMs may not occur in real materials (see for example the discussion in the final paragraph of §3). The algebraic approach is illustrated by application to perovskites, to quartz, and to the hexagonal and tetragonal tungsten bronzes; it gives results for perovskites in complete agreement with the literature (Howard & Stokes, 1998); for quartz it reveals an interesting connection between the rotational and displacive modes of the well known β to α transition; and for the tungsten bronzes it gives good agreement with structures already reported in the literature (Smirnov & Saint-Grégoire, 2014; Whittle *et al.*, 2015), and importantly, it reveals additional structures that were previously overlooked.

APPENDIX *A*
Coordinate systems for rigid-unit rotation vectors

In this work, we have used lattice units for all atomic coordinates, atomic displacements and pivot-atom rotations. The crystal-axis coordinate system is the most commonly used

system for presenting magnetic moment vectors in crystals. Because rotational and magnetic moments in crystals have strong physical and mathematical analogies, it is appropriate that we also explain how to use crystal-axis coordinates to describe rotation vectors.

Let B be the matrix whose columns are the Cartesian coordinates of the basis vectors of the unit cell, and let L be the diagonal matrix whose diagonal elements are the lengths of the three cell edges. Both B and L have Å units. For the case of orthogonal crystal axes, B is diagonal so that $B = L$.

Rotation-vector components ($\mathbf{r}_{\rm latt}$) in the crystal-axis coordinate system are related to those of the Cartesian ($\mathbf{r}_{\rm cart}$) and lattice coordinate ($\mathbf{r}_{\rm cryst}$) systems as follows below. Note that atomic displacements transform using the same equations:

$$\mathbf{r}_{\rm latt} = B^{-1} \cdot \mathbf{r}_{\rm cart} = L^{-1} \cdot \mathbf{r}_{\rm cryst}$$

$$\mathbf{r}_{\rm cart} = B \cdot \mathbf{r}_{\rm latt} = B \cdot L^{-1} \cdot \mathbf{r}_{\rm cryst}$$

$$\mathbf{r}_{\rm cryst} = L \cdot \mathbf{r}_{\rm latt} = L \cdot B^{-1} \cdot \mathbf{r}_{\rm cart}.$$

All three systems have advantages and disadvantages. Cartesian vector components always have the physically expected units. Cartesian basis vectors are orthonormal, though they do not all align with the unit-cell basis vectors when non-90° angles are present. Lattice coordinates basis vectors always align with the unit-cell basis vectors. Lattice coordinate vector components are conveniently unitless for atomic coordinates, but have unfamiliar units for other quantities (*e.g.* radians/Å for rotations and μB/Å for magnetic moments); they also suffer from a dependence on the cell parameters of the crystal, even when the physical vector (*e.g.* rotation or displacement) itself is constant. Crystal-axis coordinates are a partial compromise between the Cartesian and lattice coordinate systems. Crystal-axis basis vectors always align with the unit-cell basis vectors. Crystal-axis vector components always have the physically expected units, and are not dependent on the cell-edge parameters of the crystal; but they do depend on the unit-cell angles, which can be an annoyance.

For the perovskite example, the actual rotational symmetry-mode amplitudes of the R_4^+, X_5^+ and M_3^+ modes are approximately −0.0700, 0 and 0.0572 rad, respectively, which are also the components of vector **A**. The vector **S** can then be calculated as

$$\mathbf{S} = \mathbf{T}_A \cdot \mathbf{A} = \begin{pmatrix} -0.08839 & 0 & 0 \\ 0 & 0 & 0.0625 \\ 0 & 0.08839 & 0 \end{pmatrix} \begin{pmatrix} -0.0700 \\ 0 \\ 0.0572 \end{pmatrix} = \begin{pmatrix} 0.00619 \\ 0.00358 \\ 0 \end{pmatrix}.$$

In this example, **S** contains all three rotational components of a single Mn pivot atom, so that it is essentially the same as $\mathbf{r}_{\rm latt}$, expressed in radians/Å units. Because the child cell is a $2^{1/2} \times 2 \times 2^{1/2}$ supercell of a 4 Å cubic parent cell, the matrix B has $4(2^{1/2})$ Å, 8 Å and $4(2^{1/2})$ Å on the diagonal. And because the unit-cell axes are all orthogonal, $B = L$, so that $\mathbf{r}_{\rm cart} = \mathbf{r}_{\rm cryst} = B \cdot \mathbf{r}_{\rm latt}$ $[4(2^{1/2})](0.00619, 0.00358, 0) = (0.0350, 0.0286, 0)$, expressed in radian units. The magnitude of this vector is then $(0.0350^2 + 0.0286^2)^{1/2} = 0.0452$ radians or 2.59°.

References

Ainger, F. W., Bickley, W. P. & Smith, G. V. (1970). *Proc. Br. Ceram. Soc.* **18**, 221–237.
Aleksandrov, K. S. (1976). *Ferroelectrics*, **14**, 801–805.
Benedek, N. A., Rondinelli, J. M., Djani, H., Ghosez, P. & Lightfoot, P. (2015). *Dalton Trans.* **44**, 10543–10558.
Bobb, L. C., Lefkowitz, I. & Muldawer, L. (1969). *J. Appl. Cryst.* **2**, 189–190.
Bradley, C. J. & Cracknell, A. P. (1972). *The Mathematical Theory of Symmetry in Solids.* Oxford: Clarendon.
Campbell, B. J., Stokes, H. T., Tanner, D. E. & Hatch, D. M. (2006). *J. Appl. Cryst.* **39**, 607–614.
Carpenter, M. A. & Salje, E. K. H. (1998). *Eur. J. Mineral.* **10**, 693–812.
Carpenter, M. A., Salje, E. K. H. & Graeme-Barber, A. (1998). *Eur. J. Mineral.* **10**, 621–691.
Chi, E. O., Gandini, A., Ok, K. M., Zhang, L. & Halasyamani, P. S. (2004). *Chem. Mater.* **16**, 3616–3622.
Debnath, T., Roy, S. C., Rüscher, C. H. & Hussain, A. (2009). *J. Mater. Sci.* **44**, 179–185.
Dove, M. T. & Fang, H. (2016). *Rep. Prog. Phys.* **79**, 066503.
Francombe, M. H. & Lewis, B. (1958). *Acta Cryst.* **11**, 696–703.
Giddy, A. P., Dove, M. T., Pawley, G. S. & Heine, V. (1993). *Acta Cryst.* A**49**, 697–703.
Glazer, A. M. (1972). *Acta Cryst.* B**28**, 3384–3392.
Goldschmidt, V. M. (1926). *Naturwissenschaften*, **14**, 477–485.
Goreaud, M., Labbé, Ph., Montfort, Y. & Raveau, B. (1980). *Rev. Chim. Miner.* **17**, 79–87.
Hammonds, K. D., Dove, M. T., Giddy, A. P. & Heine, V. (1994). *Am. Mineral.* **79**, 1207–1209.
Hatch, D. M. & Ghose, S. (1991). *Phys. Chem. Miner.* **17**, 554–562.
Haydon, S. K. & Jefferson, D. A. (2002). *J. Solid State Chem.* **168**, 306–315.
He, J., Borisevich, A., Kalinin, S. V., Pennycook, S. J. & Pantelides, S. T. (2010). *Phys. Rev. Lett.* **105**, 227203.
Heaney, P. J. & Veblen, D. R. (1991). *Am. Miner.* **76**, 1018–1032.
Howard, C. J., Campbell, B. J., Stokes, H. T., Carpenter, M. A. & Thomson, R. I. (2013). *Acta Cryst.* B**69**, 534–540.
Howard, C. J. & Stokes, H. T. (1998). *Acta Cryst.* B**54**, 782–789.
Howard, C. J. & Stokes, H. T. (2005). *Acta Cryst.* A**61**, 93–111.
Jamieson, P. B., Abrahams, S. C. & Bernstein, J. L. (1968). *J. Chem. Phys.* **48**, 5048–5057.
Jamieson, P. B., Abrahams, S. C. & Bernstein, J. L. (1969). *J. Chem. Phys.* **50**, 4352–4363.
Kihlborg, L. & Klug, A. (1973). *Chem. Scr.* **3**, 207–211.
Labbé, Ph., Leligny, H., Raveau, B., Schneck, J. & Tolédano, J. C. (1989). *J. Phys. Condens. Matter*, **2**, 25–43.
Lay, D. C. (1997). *Linear Algebra and its Applications.* Reading: Addison Wesley.
Le Page, Y. & Donnay, G. (1976). *Acta Cryst.* B**32**, 2456–2459.
Levin, I., Stennett, M. C., Miles, G. C., Woodward, D. I., West, A. R. & Reaney, I. M. (2006). *Appl. Phys. Lett.* **89**, 122908.
Lufaso, M. W. & Woodward, P. M. (2001). *Acta Cryst.* B**57**, 725–738.
Magnéli, A. (1949). *Ark. Kemi*, **1**, 213–221.
Megaw, H. D. (1973). *Crystal Structures – a Working Approach.* Philadelphia: W. B. Saunders.
Neurgaonkar, R. R., Nelson, J. G. & Oliver, J. R. (1992). *Mater. Res. Bull.* **27**, 677–684.
Prinz, H., Müller, U. & Ha-Eierdanz, M.-L. (1992). *Z. Anorg. Allg. Chem.* **609**, 95–98.
Pryde, A. K. A. & Dove, M. T. (1998). *Phys. Chem. Miner.* **26**, 171–179.

Rodríguez-Carvajal, J., Hennion, M., Moussa, F., Moudden, A. H., Pinsard, L. & Revcolevschi, A. (1998). *Phys. Rev. B*, **57**, R3189–R3192.
Shirane, G. & Yamada, Y. (1969). *Phys. Rev.* **177**, 858–863.
Smirnov, M. & Saint-Grégoire, P. (2014). *Acta Cryst.* A**70**, 283–290.
Steadman, R. (1972). *Mater. Res. Bull.* **7**, 1143–1150.
Stennett, M. C., Reaney, I. M., Miles, G. C., Woodward, D. I., West, A. R., Kirk, C. A. & Levin, I. (2007). *J. Appl. Phys.* **101**, 104114.
Stokes, H. T. (2006). *Introduction to Isotropy Subgroups and Displacive Phase Transitions.* In *ISOTROPY* software suite (http://iso.byu.edu/iso/isotropy.php).
Stokes, H. T., van Orden, S. & Campbell, B. J. (2016). *J. Appl. Cryst.* **49**, 1849–1853.
Stoumpos, C. C., Malliakas, C. D. & Kanatzidis, M. G. (2013). *Inorg. Chem.* **52**, 9019–9038.
Subbarao, E. C., Shirane, G. & Jona, F. (1960). *Acta Cryst.* **13**, 226–231.
Swainson, I. P. & Dove, M. T. (1993). *Phys. Rev. Lett.* **71**, 193–196.
Takusagawa, F. & Jacobson, R. A. (1976). *J. Solid State Chem.* **18**, 163–174.
Talanov, V. M. & Shirokov, V. B. (2012). *Acta Cryst.* A**68**, 595–606.
Triantafyllou, S. T., Christidis, P. C. & Lioutas, Ch. B. (1997). *J. Solid State Chem.* **130**, 176–183.
Wachsmann, C. & Jacobs, H. (1995). *Eur. J. Solid State Inorg. Chem.* **32**, 1023–1025.
Whitfield, P. S., Herron, N., Guise, W. E., Page, K., Cheng, Y. Q., Milas, I. & Crawford, M. K. (2016). *Sci. Rep.* **6**, 35685.
Whittle, T. A., Brant, W. R., Withers, R. L., Liu, Y., Howard, C. J. & Schmid, S. (2018). *J. Mater. Chem. C*, doi: 10.1039/C8TC00732B.
Whittle, T. A., Schmid, S. & Howard, C. J. (2015). *Acta Cryst.* B**71**, 342–348.
Withers, R. L., Tabira, Y., Liu, Y. & Höche, T. (2002). *Phys. Chem. Miner.* **29**, 624–632.
Woodward, P. M. (1997*a*). *Acta Cryst.* B**53**, 32–43.
Woodward, P. M. (1997*b*). *Acta Cryst.* B**53**, 44–66.
Wright, A. F. & Lehmann, M. S. (1981). *J. Solid State Chem.* **36**, 371–380.